TECHNICAL REPORT
https://doi.org/10.1038/s41556-021-00815-6

nature cell biology

Super-resolved 3D tracking of cargo transport through nuclear pore complexes

Rajdeep Chowdhury[1,2], Abhishek Sau[1,2] and Siegfried M. Musser[1]✉

Nuclear pore complexes (NPCs) embedded within the nuclear envelope mediate rapid, selective and bidirectional traffic between the cytoplasm and the nucleoplasm. Deciphering the mechanism and dynamics of this process is challenged by the need for high spatial and temporal resolution. We report here a multicolour imaging approach that enables direct three-dimensional visualization of cargo transport trajectories relative to a super-resolved octagonal double-ring structure of the NPC scaffold. The success of this approach is enabled by the high positional stability of NPCs within permeabilized cells, as verified by a combined experimental and simulation analysis. Hourglass-shaped translocation conduits for two cargo complexes representing different nuclear transport receptor pathways indicate rapid migration through the permeability barrier on or near the NPC scaffold. Binding sites for cargo complexes extend more than 100 nm from the pore openings, which is consistent with a wide distribution of the phenylalanine-glycine polypeptides that bind nuclear transport receptors.

The NPCs perforating the nuclear envelope (NE) enable the nucleocytoplasmic exchange of ~1,000 molecules per NPC per second[1] with typical protein transit times of ~10 ms (refs. [2–4]). How the permeability barrier is able to selectively accommodate cargos with dramatically different physical characteristics (for example, from small proteins to pre-ribosomal subunits) moving in both directions is a heavily studied but still unsolved problem[5,6]. An attractive notion is that distinct high probability paths through the permeability barrier exist for the different nuclear transport receptor (NTR)-dependent pathways, and that these could be segregated for import and export[7–9]. While evidence exists for some partial separation of transport paths, overlap also exists[10,11]. Binding assays, sequence analysis and structure modelling predict that NTR binding motifs are asymmetrically distributed within the permeability barrier, which is consistent with the notion of distinct translocation conduits[12–15]. Although electron microscopy reveals high-resolution snapshots of translocation events and simultaneously visualizes the translocation pore[10,16], it lacks the capability to visualize rapid dynamics in three dimensions. Three-dimensional (3D) models of transport pathways have been deduced from two-dimensional (2D) light microscopy videos[11,17]. However, the direct 3D tracking of cargo translocation with high time-resolution in the context of well-resolved NPCs necessary to accurately decipher the geometrical and physical properties of translocation conduits has not been reported.

The human NPC scaffold has an outer diameter of ~110 nm, and the hourglass-shaped central pore has a minimum constriction of ~50 nm (refs. [18,19]). Nonetheless, the NPC is largely impermeable to molecules larger than ~4–5 nm that are not bound to NTRs[20,21]. The permeability barrier is generated by a network of ~200–250 largely intrinsically disordered polypeptide chains that occupy the central pore and decorate its cytoplasmic and nucleoplasmic openings[14,22]. These disordered polypeptides contain, in aggregate, 3,000–4,000 phenylalanine-glycine (FG) repeats to which NTRs transiently bind as they carry cargos through NPCs[14,23–25]. Both peripheral and central translocation pathways through this FG network have been identified[11,26], although the rules by which cargo complexes partition into distinct locales and the extent to which pathways overlap remains unsettled. Our goal was to develop an approach that would allow us to characterize the real-time dynamics of cargo translocation in the context of a well-resolved NPC scaffold. In most super-resolution imaging studies of NPC scaffold structures reported to date, NEs were stabilized via fixation (for examples, see refs. [27–30]), thus eliminating the possibility of exploring the dynamics of key aspects of the translocation process. We demonstrate here using non-fixed NEs that NPCs are sufficiently positionally stable over ~10 min in permeabilized cells such that 3D transport trajectories can be aligned with a highly resolved NPC scaffold with eightfold rotational symmetry. We therefore report a substantially improved approach for investigating the dynamics of nucleocytoplasmic transport.

Results

Overview of the experimental design. While numerous 3D light microscopy methods have been developed over the last few decades, single-molecule astigmatism imaging[31] provides high temporal resolution from a single image, high spatial precision in *x*, *y* and *z*, and its useful *z*-range matches well to that necessary to monitor cargo trafficking through NPCs[32,33]. Although the simplest approach to achieve astigmatism imaging is via a cylindrical lens[31], we used an adaptive optic (AO) system (Fig. 1a), which enabled optimization of the astigmatism for the needs of the experiment as well as correction of the focal mismatch arising from chromatic aberrations in multicolour applications. Fluorescence was recovered from NPCs within the largely flat bottom NE of the nuclei of permeabilized U-2 OS cells (Fig. 1b) using a narrow-field epifluorescence scheme[2]. NPCs tagged on NUP96 with monomeric enhanced green fluorescent protein (mEGFP) were first decorated with dye-labelled anti-GFP nanobodies, and then transport mix was added to begin the import experiments. The NPC scaffold and cargo complexes were imaged separately but sequentially with no reagent changes (Fig. 1c). Individual fluorescent spots were localized with *z*-dependent and photon-count-dependent localization precision in each of the three dimensions (Fig. 1d–f).

[1]Department of Molecular and Cellular Medicine, Texas A&M University, College of Medicine, The Texas A&M Health Science Center, College Station, TX, USA. [2]These authors contributed equally: Rajdeep Chowdhury, Abhishek Sau. ✉e-mail: smusser@tamu.edu

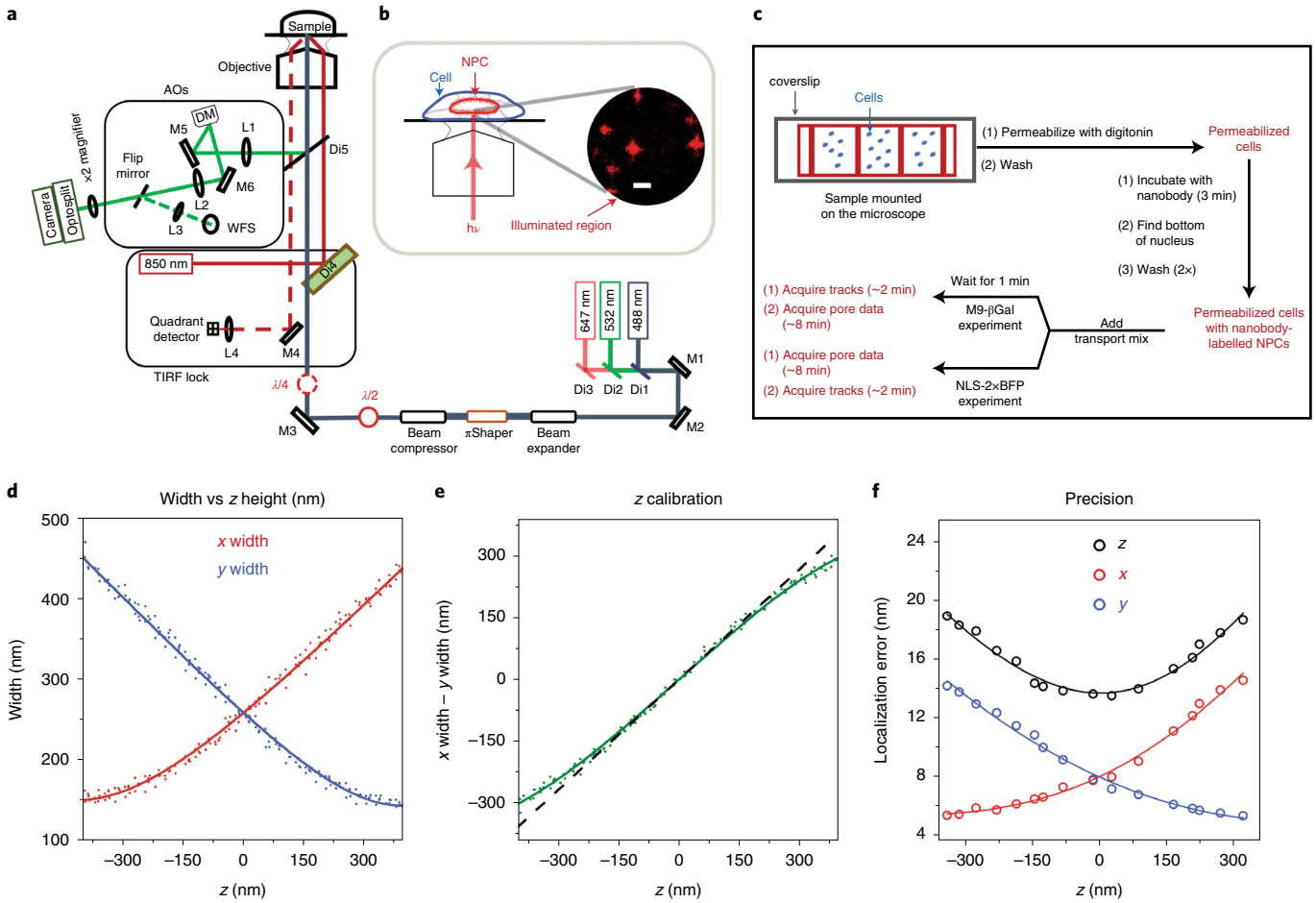

Fig. 1 | 3D super-resolution microscope and experimental workflow. a, The 3D microscope set-up used to obtain super-resolved positional information for single dyes on the NPC scaffold and for individual diffusing cargo complexes. Fluorescence was collected by an EMCCD camera after passing through a home-built AO system (AOs). The deformable mirror (DM) was used to first correct optical aberrations via a feedback algorithm with the wavefront sensor (WFS) and then to introduce the astigmatism needed for 3D imaging. A self-configured TIRF-lock system ensured a *z* stability of <3 nm. Lenses (L), mirrors (M) and dichroic mirrors (Di) are indicated. **b**, Schematic of the imaging plane. The bottom surface of nuclei contained NPCs within a nearly flat NE that was perpendicular to the narrow-field illumination beam. The image shows the fluorescence from single HMSiR dye molecules on NPCs (Fig. 2) using astigmatism imaging, in which *z* information is retrieved from the elongation of the spot in *x* or *y*. Scale bar, 1 µm. **c**, Experimental workflow. The total time for sample preparation and data acquisition was ~20 min after cell permeabilization. Data collection at room temperature required ~10 min via approach 1 (cargo complexes tracked first, NPCs localized second) or approach 2 (reverse order). **d**–**f**, Microscope *z* calibration and precision using a 60 nm root mean square (r.m.s.) astigmatism introduced with the DM. The *z* dependence of *x* and *y* spot widths (**d**) was obtained from *z*-stack images (100 ms frame^{-1}, 41 steps, step size of 25 nm) of five different 0.1-µm beads embedded in 2% agarose (λ_{ex} = 647 nm; ~2,500–3,500 photons per spot). The difference between the *x* and *y* widths was approximately linearly dependent on *z* (**e**, dashed black line). The fits in **d** and **e** have been previously described[31], although the *z* calibration data obtained for NPCs used the improved algorithm implemented in ThunderStorm[66]. The localization errors (precision values) were defined as the standard deviation of the position in *x*, *y* and *z* over 100 images of 0.1-µm beads embedded in 2% agarose (**f**). Precision values obtained at various excitation intensities (~1,500–4,500 photons per spot; 50 ms frame^{-1}), and *z* positions were scaled to the 3,000 photon level by multiplication by $(N_p/3{,}000)^{1/2}$, where N_p is the number of photons, and were fit with equation (5), equation (6) and equation (7b). These data illustrate that the three spatial measurement precision values for each fluorescent spot depends on the photons collected and the position in *z*. See Methods for additional details. Source numerical data are provided in source data.

A highly resolved NPC scaffold in 3D. An averaged eightfold rotationally symmetric NPC scaffold was obtained as described in Fig. 2. Nanobodies[34] tagged with the spontaneous blinking dye HMSiR[35] were bound to the mEGFP domains on chromosomally expressed NUP96–mEGFP[28] (Fig. 2a–d, Extended Data Fig. 1a and Supplementary Video 1). Fluorescent spots arising from HMSiR molecules were curated to those with $N \geq 3{,}000$ photons, which yielded initial super-resolved images of NPCs (Fig. 2e). Clusters arising from at least ten spots were fit to a double-circle distribution (Fig. 2f,g). Clusters surviving the double-circle fitting routine—that is, with centroids of $z = 0 \pm 200$ nm, diameters of 80–135 nm and ring spacing of 40–65 nm—were considered well-localized NPCs (Fig. 2h and Extended Data Fig. 2). The photon and *z* selection applied yielded average single particle precision values of ~7 nm in *x* and *y* and ~12 nm in *z*. These precision values are the weighted statistical averages considering the photon and *z* distributions for the final curated localizations (calculated with Supplementary Data 1 (software file 1) using the data in Fig. 1f over the volume and photon levels analysed). Initial cluster alignments of well-localized NPCs, assuming no tilt from the *z* axis, yielded a clear double-ring structure (Fig. 2i,j), which is consistent with the known positions of the 32 molecules of NUP96 within the NPC scaffold (Fig. 2a).

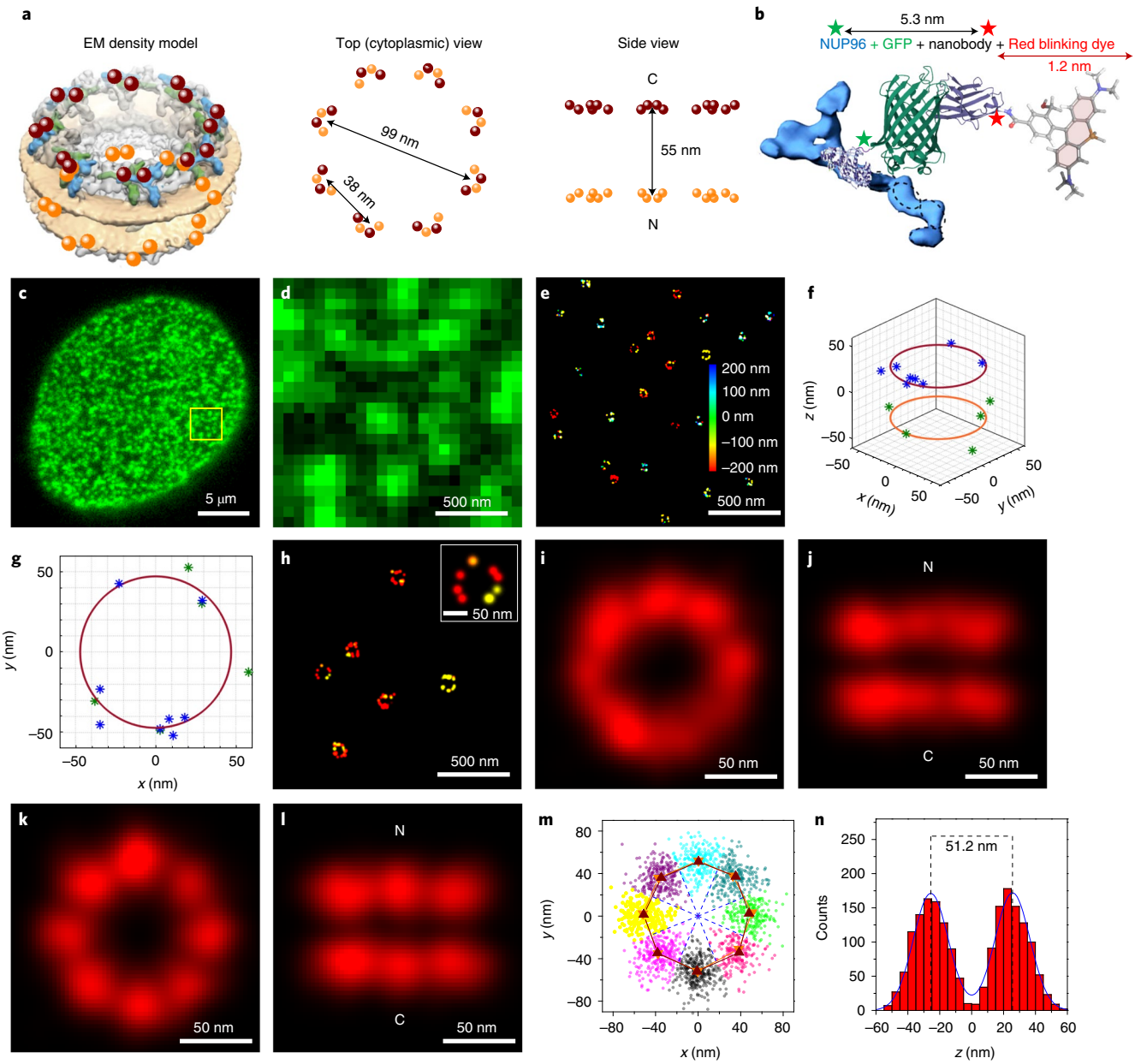

Fig. 2 | Localization of the NPC scaffold. a, Schematic of the NUP96 distribution within NPCs. The maroon and orange dots (cytoplasmic (C) and nucleoplasmic (N) rings, respectively) indicate the 3D position of the C termini of the 32 NUP96 molecules within the electron microscopy (EM) density map (EMD-3103)[67]. **b**, The HMSiR blinking dye labelling approach of the mEGFP domain on NUP96 (not to scale). **c**,**d**, Wide-field fluorescence emission image of mEGFP from the bottom NE of a permeabilized U-2 OS-CRISPR-NUP96-mEGFP[28] cell (λ_{ex} = 488 nm). Spots (green) are individual NPCs. Similar results were observed for N = 100 cells. Panel **d** represents an expanded view of the square region identified in **c**. **e**, First-pass images of individual super-resolved NPCs. These dye clusters remained after applying photon and z filters. The colour bar represents the z height. The total acquisition time per nucleus was ~8 min (50 ms frame^{-1}, λ_{ex} = 647 nm, 3 kW cm^{-2}). **f**,**g**, Representative double-circle fit for determining NPC centroids. **h**, 3D super-resolution images of individual well-localized NPCs. These clusters survived the double-circle fitting routine and were selected for alignment into the NPC scaffold. See Extended Data Fig. 2 for the selection workflow. **i**,**j**, Composite NPC images from aligned but unrotated clusters (1,872 localizations obtained from 142 clusters from 10 nuclei; each nucleus was an independent biological replicate). **k**,**l**, Composite NPC images from rotated clusters revealing the eightfold rotational symmetry. These images were constructed from a single dataset. Images from a duplicate dataset are shown in Fig. 5a,b, and a quantitative comparison is provided in Table 1. See Supplementary Video 2 for rotated views. **m**, Localizations from all NPCs separated into eight segments for each ring based on an angular global fit (Extended Data Fig. 3). The angular centroid within each segment was calculated from a sinusoidal fit to the angle distribution. The difference between the angular centroids of the two rings for the eight segments is 0.9 ± 3.8°. **n**, The distribution of z values from all NPCs. The symmetric double Gaussian fit (centred at 0) indicates that the distance between the two rings is 51.2 nm. Simulated distributions and errors are modelled in Fig. 3. Source numerical data are provided in source data.

The angles of individual localizations relative to the cluster centroid were estimated and binned (0–45°), assuming an eightfold rotationally symmetric distribution. The estimated phase angle was then used to realign the individual pore clusters, which resulted in an easily recognizable eightfold symmetrical structure in both rings (Fig. 2k,l and Supplementary Video 2), which is consistent with

structural studies[18,19]. Despite the poor angle fits due to the low number of points distributed in 5° bins, this approach worked well (Extended Data Fig. 3). The ring radius of 52.4 nm (Fig. 2m) and ring spacing of 51.2 nm (Fig. 2n) agree well with the known positions of NUP96 (Fig. 2a), especially considering the 6–7 nm distance between the dye and the NUP96 attachment point (Fig. 2b).

Positional stability of the NPCs. The total time over which localizations for individual NPCs was collected was ~8 min, which provided ample opportunity for the NPCs to move within the NE or for the NE itself to undergo large-scale fluctuations. To better understand the errors in the generated scaffold structures (Fig. 2k,l), we simulated distributions of stochastically distributed NUP96 localizations based on potential sources of error and experimentally determined constraints. In addition to the experimentally determined x, y and z localization errors (σ_x, σ_y and σ_z), potentially important error sources are the cluster centroid localization errors (σ_{cx}, σ_{cy} and σ_{cz}), the axial tilt of the NPC (σ_{at}) and the NE/NPC positional (cartesian) instability (collectively termed the 'jiggle'). That is, the axial fluctuations in NE/NPC position (σ_{NPCz}) and the lateral NPC movements within the NE (σ_{NPCx} and σ_{NPCy}). Physical instability errors (for example, chamber movements) are assumed to be subsumed into the localization errors. A comparison of z and radial distribution widths obtained for experimental and simulated data revealed that the axial tilt is less than or equal to ~10°, the jiggles in x and y are less than ~8–9 nm and the axial NE/NPC fluctuations are less than ~6 nm (Fig. 3). The positional immobility of NPCs within the NE is well known, enabled by the nuclear lamin structure[36], and essential for the success of particle-tracking measurements on transiting cargos[2,37]. The comparison of experimental and simulated data reported here provides quantitative limits on NPC movements within permeabilized cells. Since the NE is more mobile in live cells[38], a substantial increase in the stability of the system must have ensued as a result of the permeabilization procedure and the subsequent wash steps. These procedures removed the bulk of the soluble material, including the energy and regulatory systems responsible for controlling cytoskeletal polymerization and depolymerization. Since the nuclei were not directly attached to the glass coverslip, stabilized cytoskeletal filaments probably contributed to providing structural stability to the NE.

Cargo-complex tracking strategies. Owing to the high positional stability of NPCs, we used a two-colour approach to combine the well-localized NPCs with 3D particle trajectories of cargo complexes undergoing transport. As indicated in Fig. 1c, the NPC scaffold data were either collected before or after the cargo transport data. In both cases, the only changes to switch between imaging modes were software-driven changes in illumination wavelength and an AO chromatic correction (Methods). These two approaches had distinct advantages and disadvantages. When cargo transport was imaged first (approach 1), nuclear background fluorescence was low since the transport reaction was recently initiated. However, the camera integration time for the cargo trajectories was minimally ~3 ms, as the higher 532 nm excitation intensities required for faster image acquisition resulted in unacceptable photobleaching of the HMSiR dye, which was visualized later. In contrast, when the NPC scaffold data were obtained first (approach 2), acquisition speed during cargo imaging was limited by the photon collection efficiency of the system. However, substantial background fluorescence arose from inside the nucleus from already imported molecules, which therefore required photobleaching before the signal-to-noise ratio was high enough for data collection. For approach 1, we followed the strategy of our previous work[39], beginning the accumulation of trajectory data ~1 min after the cargo, transport factors and RanGTP (transport mix) were added and continuing for ~2 min. After collecting the cargo trajectory data, we then switched to localization of the NPC scaffolds for ~8 min. For approach 2, scaffold data collection (~8 min) began shortly after the addition of the transport mix, and when completed, cargo trajectory data were collected (~2 min). In both cases, the total time elapsed for data collection in an individual experiment was ~10 min, although data acquisition was delayed for ~1 min for approach 1, as indicated earlier. The mEGFP fluorescence was photobleached by ~2 s of 532 nm excitation (Extended Data Fig. 1b) before collecting cargo trajectory data.

Approach 1: import of M9-βGal/transportin complexes. We first examined transport of a previously characterized large tetrameric model cargo, M9-βGal (~500 kDa; full name M9-βGal-8C)[40] labelled with Atto542 on the eight accessible cysteine residues. M9-βGal(Atto542) requires the transportin NTR for import (Extended Data Fig. 4). Single-molecule transport experiments were conducted in the presence of an excess of transportin. The M9-βGal cargo tracking strategy is illustrated in Fig. 4 and Supplementary Videos 3 and 4. Owing to the narrow-field illumination scheme[2] used, diffusing cargo complexes underwent a degree of photobleaching before encountering a NPC. Consequently, spots were curated to those with $N \geq 1{,}000$ photons, which yielded average single-particle precision values of ~12 nm in x and y and ~21 nm in z. All cargo localizations within a 400 nm cube centred on an NPC centroid were identified and aligned to the averaged NPC scaffold, using the same rotational matrix used for the NPC that the cargo was associated with (Fig. 4a,b). The NPC scaffold data in Fig. 4 are the same as that reported in Fig. 2 as these NPC data were collected immediately after the M9-βGal cargo trajectory data. As freely diffusing molecules were expected to be only transiently present, whereas cargo complexes that interact with NPCs were expected to have an average residence time of ~9 ms (ref. [40]), we curated the data to include only those molecules present for

Fig. 3 | Effect of tilt and jiggle on resolving the NPC scaffold. a, An expanded version of the dataset used to construct Fig. 2k,l. For comparison with the simulations, these data underwent less selection before rotationally corrected alignment (corresponding to the clusters in Extended Data Fig. 3c without filtering the diameter and the distance between the rings, but with a z centroid of 0 ± 200 nm). Therefore, there are significantly more localizations (N = 2,362 localizations from 181 clusters) than in Fig. 2k,l; the distribution of localizations/cluster is given in Extended Data Fig. 2e. The radial width (σ_{rw}) and z width (σ_{zw}) are key parameters for comparing distributions and reflect standard deviations of Gaussian and symmetric double Gaussian fits, respectively. **b**,**c**, Effect of tilt and jiggle. Average (±s.d.) radial widths (**b**) and z widths (**c**) from 20 independent simulations. The horizontal black dashed lines indicate the experimental radial and z widths from **a**, and the red lines indicate these values for the localization data used to make Fig. 2k,l. The data in **c** indicate that the tilt is ≤~10°, and the total jiggle in z is < ~6 nm. While the x, y and z jiggles were identical in **b** and **c**, they largely independently influence the radial or z width. With this in mind, the jiggles in x and y are 8–9 nm (**b**). **d**–**f**, Simulated distributions based on various jiggle and tilt values. As an initial reference, a simulated distribution with no tilt or jiggle (**d**) reveals the expected data scatter based on the current localization precision. Considering the results in **b** and **c**, a minimal non-zero z jiggle of 3 nm was assumed, which suggested a maximum reasonable tilt of 9° and x and y jiggles of 8 nm (**e**). Alternatively, considering that the z jiggle is potentially larger, a more moderate tilt (5°) suggests a z jiggle of 5 nm and x and y jiggles of 9 nm (**f**). Both **e** and **f** reasonably reproduced the experimental data. The simulations reported here do not include centroid localization errors; these would be identical in effect to the jiggles. By applying the two-circle fit algorithm to simulated data, the centroid localization errors were estimated as 4–5 nm in x, y and z. See Methods for additional details. Source numerical data are provided in source data.

three or more consecutive frames. This approach yielded a distribution (Fig. 4c,d) with a substantially clarified NE region, except at the location occupied by the pore.

The large clouds near both the cytoplasmic and nucleoplasmic openings suggested that the cargo complexes had interactions with structures far beyond the translocation pore. To further explore this

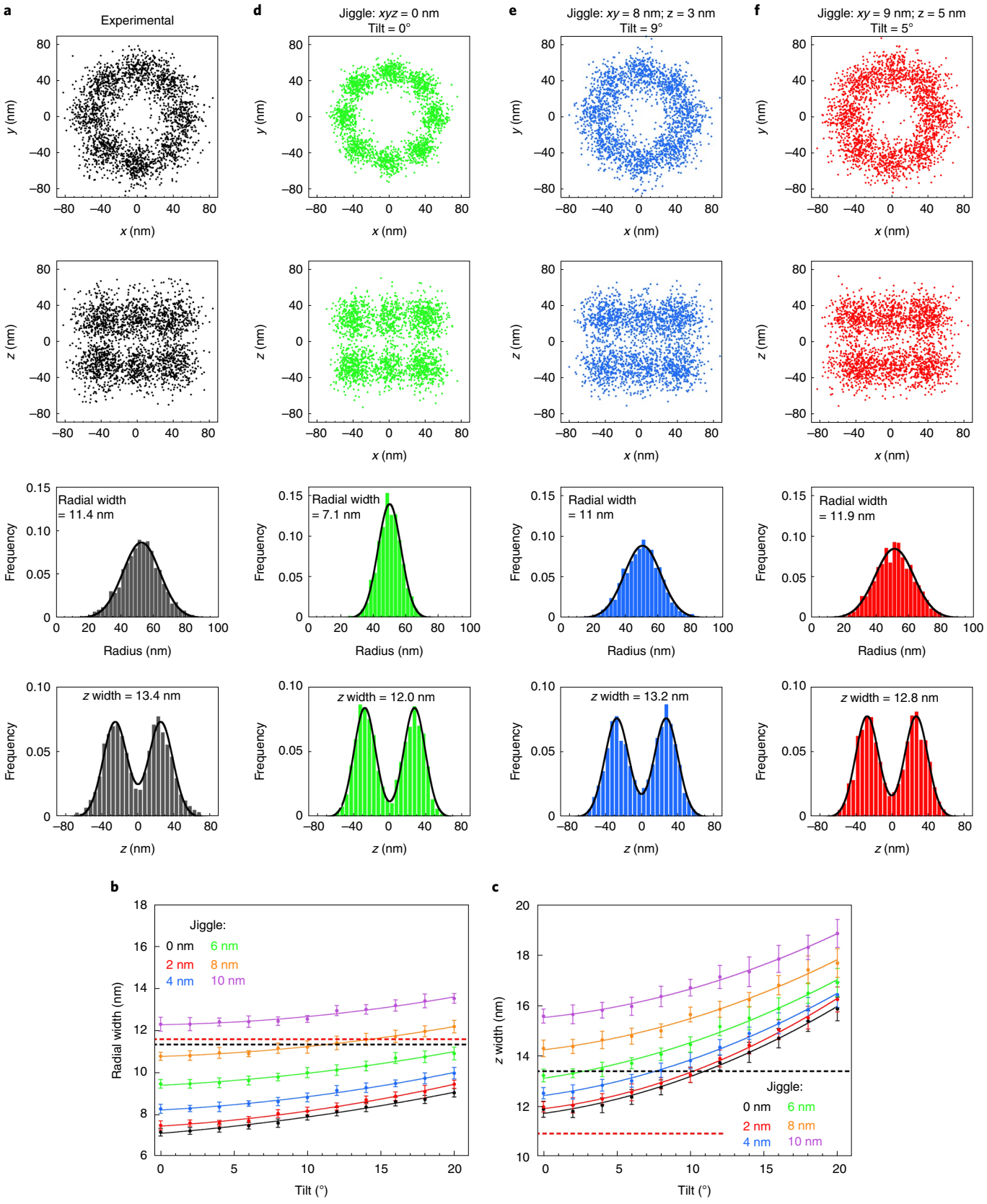

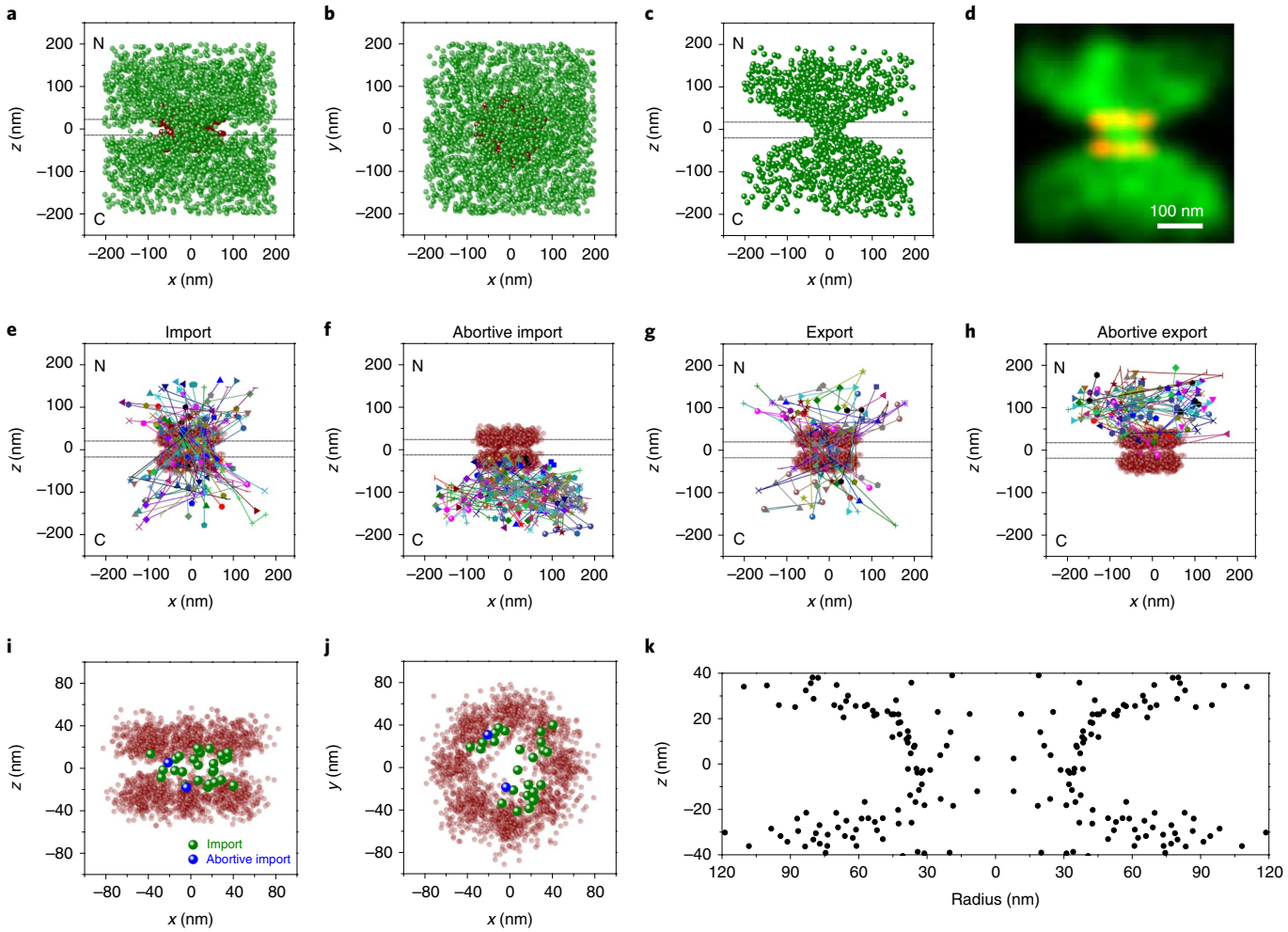

Fig. 4 | 3D tracking of M9-βGal cargo complexes interacting with and transiting through NPCs. a,**b**, All M9-βGal(Atto542) localizations ($N = 2{,}665$ localizations from 142 NPCs from 10 nuclei; each nucleus was an independent biological replicate, green) within a 400-nm cube centred on NPC clusters (from Fig. 2, red), shown from the side (**a**) and from the cytoplasm (**b**). The total acquisition time per nucleus for cargo localizations was ~2 min (3 ms frame^{-1}, $\lambda_{ex} = 532$ nm, 50 kW cm^{-2}). The two horizontal dashed lines (0 ± 20 nm) in **a**,**c**,**e**–**h** indicate the approximate location of the NE membranes. [M9-βGal(Atto542)] = 1 nM, [transportin] = 1.0 μM, [RanGDP] = 0.5 μM, [NTF2] = 1 μM, [GTP] = 1 mM. **c**,**d**, Localizations for cargos detected in three or more consecutive frames ($N = 1{,}077$ localizations selected from the data in **a**,**b**) in localization- (**c**) and Gaussian-rendered (**d**) maps. Eliminated localizations appear to be randomly distributed (Extended Data Fig. 5a,b,e). **e**–**h**, Representative trajectories. Select trajectories (from $N = 239$ trajectories obtained from the data in **a**,**b**) separately identified as import (**e**; 39%), abortive import (**f**; 27%), export (**g**; 18%) and abortive export (**h**; 16%). **i**,**j**, Distribution maps of localizations from import and abortive import trajectories within the NPC scaffold ($z = 0 \pm 20$ nm) shown from the side (**i**) and from the cytoplasm (**j**). **k**, The z-dependent radial distribution of the localizations from import and abortive import trajectories within the central pore region. Values are duplicated by reflection through $r = 0$ to generate an image representative of a pore cross-section, thus illustrating the hourglass shape of the translocation conduit. Source numerical data are provided in source data.

possibility, the interactions were separated into import and export trajectories and whether transport occurred or did not occur (Fig. 4e–h). Both abortive import and abortive export trajectories yielded broad clouds at the cytoplasmic and nucleoplasmic openings, respectively (Fig. 4f,h). These data are consistent with the presence of binding sites extending >100 nm from the scaffold double-ring structure that impede translational mobility. Such a dispersed interaction scaffold is consistent with the network of intrinsically disordered FG polypeptides, which are known to provide binding sites for NTRs[6,24,41,42] and can extend into the cytoplasmic and nucleoplasmic compartments[43–45].

Considering the large M9-βGal cargo and the absence of endogenous export factors, the observed export trajectories (18% of total; Fig. 4g) were surprising. Possible explanations for this result include (1) the NTR-free cargo can export on its own (which is unlikely as it cannot undergo import; Extended Data Fig. 4), (2) the bound transportin was not completely dissociated from M9-βGal-8C in the nucleus and so the cargo complex was re-exported, or (3) an unidentified exportin was present in sufficient quantity such that export of single cargo was detectable.

To probe the nature of the import channel, the export events were removed to generate a distribution of M9-βGal cargo localizations within the pore when entering from the cytoplasmic side (import + abortive import trajectories). While there were relatively few particle localizations obtained between the two scaffold rings, these were largely localized near the periphery of the pore (Fig. 4i,j). To further explore the nature of the translocation conduit, the radial distribution of the particles was examined in the vicinity of the pore. The radial distribution was narrowest, with the smallest average radius, near the centre of the pore (~30 nm) and wider and more diffuse (average radius > 50 nm) near the pore exits (Fig. 4k).

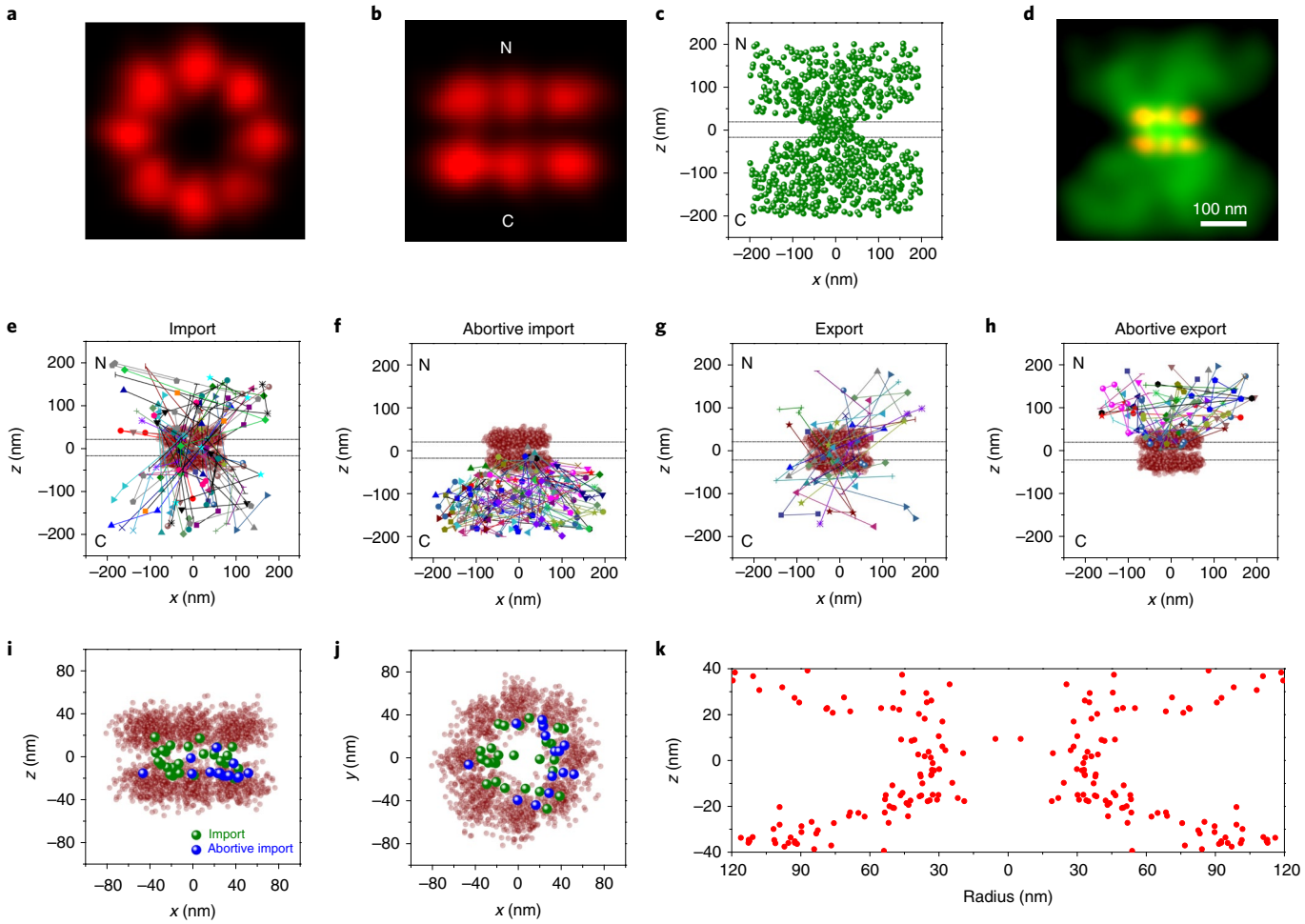

Fig. 5 | 3D tracking of NLS-2×BFP cargo complexes interacting with and transiting through NPCs. a,**b**, Composite NPC images, shown from the cytoplasm (**a**) and from the side (**b**). Visual comparison with Fig. 2k,l reveals the structural reproducibility. A quantitative comparison is given in Table 1. **c**,**d**, Localizations for NLS-2×BFP/Imp α/Imp β cargo complexes detected in three or more consecutive frames ($N = 882$ localizations from 115 NPCs from 10 nuclei; each nucleus was an independent biological replicate) in localization- (**c**) and Gaussian-rendered (**d**) maps. The total acquisition time per nucleus for cargo complex localizations was ~2 min (2 ms frame^{-1}, $\lambda_{ex} = 532$ nm, 100 kW cm^{-2}). Eliminated localizations (particles visible for 1 or 2 frames) appear to be randomly distributed (Extended Data Fig. 5c,d). The two horizontal dashed lines (0 ± 20 nm) in **c**,**e**–**h** indicate the approximate location of the NE membranes. [Imp α(Atto542)] = 1 nM, [Imp β] = 0.5 μM, [NLS-2×BFP] = 0.5 μM, [RanGDP] = 1.5 μM, [NTF2] = 1 μM, [GTP] = 1 mM. **e**–**h**, Representative trajectories. Select trajectories (from $N = 196$ trajectories selected from the data in **c**,**d**) separately identified as import (**e**; 34%), abortive import (**f**; 36%), export (**g**; 13%) and abortive export (**h**; 17%). **i**,**j**, Distribution maps of localizations from import and abortive import trajectories within the NPC scaffold ($z = 0 \pm 20$ nm) shown from the side (**i**) and from the cytoplasm (**j**). **k**, The *z*-dependent radial distribution of the localizations from import and abortive import trajectories within the central pore region (compare with Fig. 4k). Source numerical data are provided in source data.

Table 1 | Parameters for NPC scaffold localizations and cargo trajectory frequencies

Complex	Cells	NPCs	HMSiR localizations	Mean Radius, μ_r (nm)[b]	Radial width, σ_{rw} (nm)[b]	*z* spacing between rings, $2\mu_z$ (nm)[b]	*z* width, σ_{rw} (nm)[b]	Cargo trajectories per min of video[c]
M9-βGal(Atto542)/transportin	10	142	1872	52.4	11.6	51.2	10.9	18.5
NLS-2×BFP/Imp α(Atto542)/Imp β	10	115	1498	52.2	12.1	49.4	10.7	13.8
Imp α(Atto542)/Imp β	3	30	-	-	-	-	-	0[d]

[a]With the exception of the cargo trajectories per min, the first two rows were calculated from the data used to generate Figs. 2k,l and 5a,b. [b]See Fig. 3 and Methods for the definitions of terms. [c]A trajectory was defined as ≥3 sequential localizations. [d]No trajectories; 11 single points were observed.

Approach 2: import of NLS-2×BFP/Imp α/Imp β complexes. We next examined the importin α/importin β (Imp α/Imp β) pathway by monitoring the import of NLS-2×BFP/Imp α/Imp β complexes (Fig. 5 and Supplementary Videos 5 and 6). The NLS-2×BFP cargo (~57 kDa; full name NLS-2×BFP(4C)) was modelled after the previously characterized NLS-2×GFP(4C) molecule[46]. The colour of the tandem fluorescent protein was changed to eliminate the interference of weak GFP fluorescence within the cargo-complex imaging

channel (Extended Data Fig. 1b). Imp α was labelled with Atto542 on the four accessible cysteine residues[47], which resulted in a cargo complex that was approximately half as bright as the M9-βGal cargo complex. Control experiments with Imp α and Imp β alone revealed essentially no bulk import of Imp α and a substantially lower interaction frequency with NPCs than in the presence of NLS-2×BFP (Table 1 and Extended Data Fig. 4c). This was expected since the Imp β-binding domain of Imp α is autoinhibitory, i.e., it binds to the NLS binding pocket in the absence of cargo[48,49]. Thus, in the absence of cargo, Imp α cannot bind to Imp β; therefore, the localizations in Fig. 5 represent fully intact cargo complexes despite the fluorescent dyes being on Imp α. The imaging strategy was similar to that described for approach 1 (Fig. 4), except that since the NPC scaffold data were collected first, a higher time resolution could be used. The higher temporal resolution (2 ms frame^{-1}) and dimmer cargo necessitated an approximately twofold higher excitation intensity. Spots were again curated to those with $N \geq 1{,}000$ photons, which yielded average single-particle precision values similar to those observed for M9-βGal. The highly resolved octagonal double-ring structure of the NPC scaffold was reproducibly demonstrated (Fig. 5a,b and Table 1). Cargo-complex localization data were again filtered to those molecules present in the imaging region for three frames, although owing to the faster imaging speed, this corresponds to ≥6 ms (Fig. 5c,d) instead of the 9 ms threshold for approach 1. As for M9-βGal cargo complexes, large clouds near both the cytoplasmic and nucleoplasmic openings for import and export trajectories were observed (Fig. 5e–h). NLS-2×BFP cargo-complex localizations obtained within the centre of the NPC scaffold were largely localized near the periphery of the pore (Fig. 5i,j), and a radial distribution map (Fig. 5k) resembled that obtained for the M9-βGal cargo (Fig. 4k). In short, the M9-βGal and NLS-2×BFP cargo-complex tracking data yielded highly similar results.

Import pathway overlap. The M9-βGal/transportin and NLS-2×BFP/Imp α/Imp β translocation pathways were directly compared by overlaying their radial distribution maps (Fig. 6a). Since this 2D representation does not account for the larger volumes available at higher radii, volume-corrected heatmaps were generated (Fig. 6b). This analysis revealed a strong similarity between the radial distributions of the transportin and Imp α/Imp β cargo complexes within the central pore, with minor deviations and differences appearing before entering or after exiting the pore. In both cases, the cargo complexes exhibited a strong preference to transport near the NPC scaffold, minimally ~32 nm from the centre of the pore (for $z = 0 \pm 20$ nm; Fig. 6c,d). This transport near the periphery of the pore is consistent with previous results[10,11,17]. Importantly, however, the current data reveal an hourglass-shape to the translocation paths (Fig. 6). As this hourglass-shape closely resembles the inner surface of the NPC scaffold structure[15,18,19], these data are consistent with both cargo complexes diffusing along the NPC scaffold surface[50] or following a channel or annular path that is close to this surface[13,26]. Notably, our data predict a central channel width of ~60 nm, which is consistent with recent reports of 'dilated' pores (57–64 nm diameter) as a more physiologically relevant structure[51,52]. Finally, abortive import trajectories for both cargo complexes almost never penetrated the NPC midplane (Figs. 4f, 5f and 6e,f), which suggests that transport almost invariably occurred once the complex entered the central pore. In contrast, previous work indicated that molecules penetrated deeply into the FG network, even across the pore, before aborting transport[40,53]. The most probable explanation for this phenomenon is that the better localization of individual NPCs reported here provides a more accurate picture from the current data.

Discussion

In live cells, the NE undergoes shape fluctuations on the order of hundreds of nanometres in seconds[38]. In contrast, the well-resolved octagonal double-ring structure of NPCs obtained here via super-resolution imaging reveals that the NPCs and the NE are stable over ~10 min within permeabilized cells. This stability probably results from a substantial rigidification of the cytoskeletal structure(s) interacting with the NE during permeabilization. While a precise explanation for the very low mobility of NPCs requires further study, the stability of the system is remarkable, as an entirely rigid framework must exist from the coverslip, through the poly-L-lysine layer, through the fragmented plasma membrane, most probably through a stably polymerized cytoskeletal structure to the NE, which must itself prevent both lateral and axial motion of the individual NPCs. It is now apparent that fixation is not necessary for obtaining super-resolved structural information of the NPC, thereby eliminating the potential for artefacts introduced by such sample preparation, which is of particular concern for the highly flexible permeability barrier. Moreover, true 3D particle tracking of rapid real-time nucleocytoplasmic transport processes is now feasible, thereby eliminating the mathematical complications that arise when extrapolating 3D distributions from 2D data[54,55], and allowing more challenging questions to be addressed, such as relating densities to affinities, identifying discrete binding sites and determining whether transport occurs through distinct peripheral channels.

Although the NPCs in our permeabilized cells could certainly retain some NTRs and/or transport cargos, we assume that they were largely devoid of other transport traffic. Therefore, the peripheral bias that was observed for import complexes probably represents an inherent preference for this region of the permeability barrier rather than the result of competition with other transiting cargos. While the distribution of different types of FG repeat motifs (for example, FG, FxFG and GLFG) and FG density provide a probable mechanism to generate preferred translocation conduits through the FG network[7–9,15], other potential contributing mechanisms exist. For example, electrostatic potential can influence diffusional path[12], and structural organization within the permeability barrier can provide open (or, more probable, less dense) channels to bias translocation paths[13,26]. In addition, considering that the observed translocation paths seemingly follow the contour of the NPC scaffold, the potential for NTR binding sites on or near the surface of this scaffold is a reasonable consideration. The direct binding of GLFG repeats to scaffold nucleoporins[56] could contribute to ensuring that such binding sites are present. While a translocation path following the contours of the NPC scaffold is a prediction of the reduction-of-dimensionality model[50], this finding does not exclude other models[13,57–59]. However, it does challenge a prediction of the Kap-centric model, which suggests that strongly bound NTRs are embedded near the scaffold where the FG repeat density is highest, leaving a single central channel through the FG network for cargo translocation[60].

While the radial distribution data for transiting import complexes provide one constraint on the shape of the translocation conduits, the current data does not allow conclusions to be drawn regarding the angular distribution of the translocating cargo complexes relative to the NPC scaffold. Further experimental improvements are needed to distinguish between an annular-shaped translocation path or discrete channels. In the case of eight separate discrete conduits (consistent with the eightfold rotational symmetry), distinct transportin and Imp α/Imp β pathways could be maximally spaced by ~12 nm (assuming a 32 nm radius and 22.5° arc between channels). Considering that the import complexes used had average diameters of ~13 and ~8 nm (~900 kDa and ~200 kDa for the M9-βGal and NLS-2×BFP import complexes, respectively), competitive influences are expected if both cargo complexes were simultaneously transporting within neighbouring channels. Thus, despite the potential for at least a partial distinction between discrete translocation channels, high transport fluxes will undoubtedly introduce competitive effects. Competition within a single annular translocation conduit would also, of course, be expected.

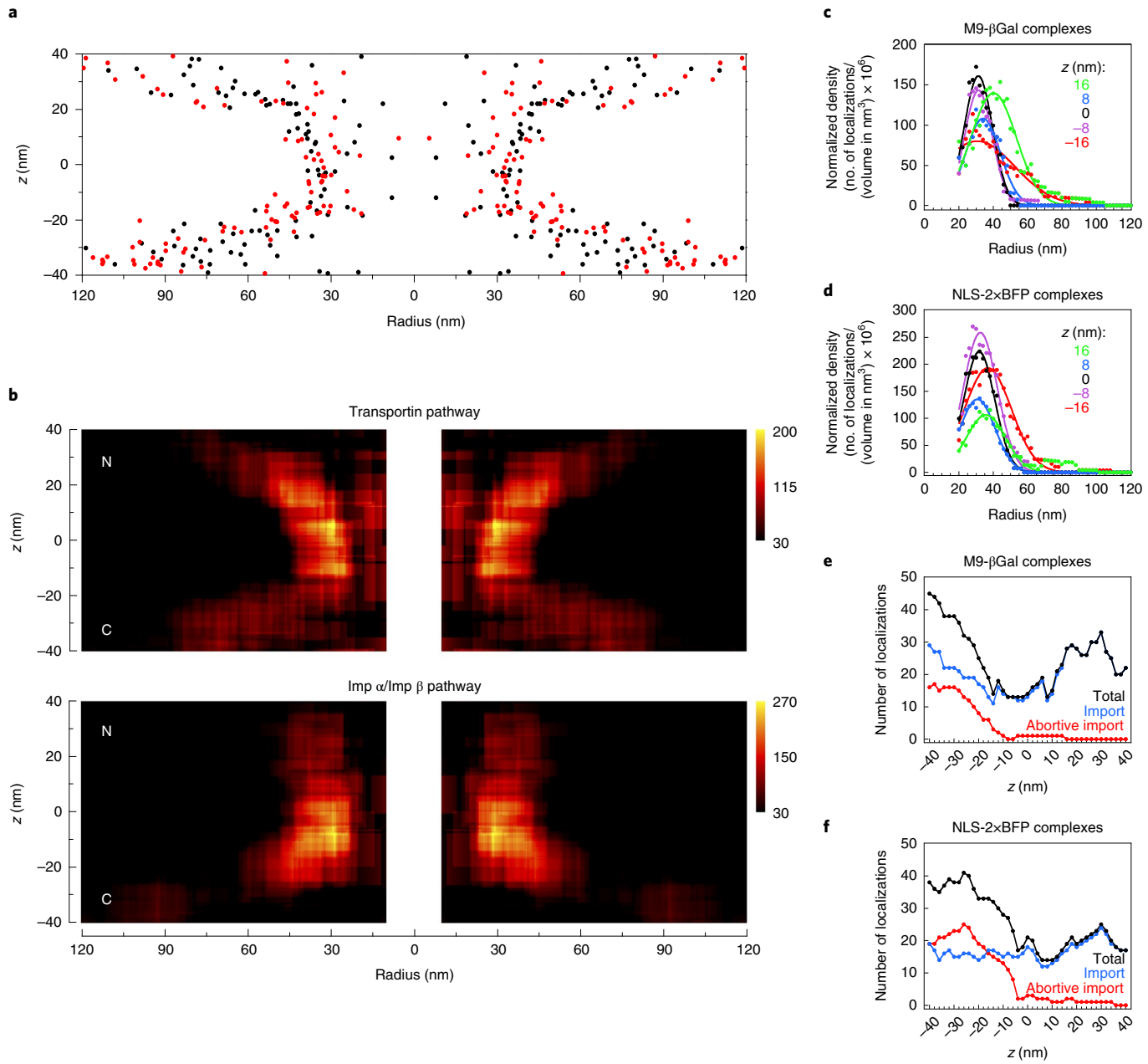

Fig. 6 | Overlap of the transportin and Imp α/Imp β import pathways. a, Overlap of *z*-dependent radial distribution maps. Data are from Fig. 4k (black, M9-βGal import complexes) and Fig. 5k (red, NLS-2×BFP import complexes). **b**, Volume-corrected heatmaps for the transportin (top) and Imp α/Imp β import (bottom) pathways. The particle distributions in **a** were volume-corrected by calculating the particle densities within annular cylinders. At each (*r*,*z*) coordinate, the number of localizations within an annular cylinder ($r = \pm 10$ nm and $z = \pm 10$ nm) were determined and divided by the total volume of the region to yield the density. The colour scale represents the particle density (number of localizations per volume in $nm^3 \times 10^6$). **c**,**d**, Radial density distributions at different *z* heights. Data from **b** were plotted for the indicated *z* values and fit with a Gaussian function. While a few localizations were observed at small radii, individual localizations in such locations had large effects on density values due to the small volumes; these values were deemed unreliable and therefore were eliminated from the analysis. For both cargo complexes, the peak density for $z = 0 \pm 20$ nm is at $r \approx 32$ nm. **e**,**f**, Number of localizations in different *z* sections for M9-βGal import complexes (**e**) and NLS-2×BFP import complexes (**f**). The total number of localizations obtained within 20-nm thick *z* sections (over all radii) are indicated. These data indicate that cargo complexes that abort transport are largely rejected before the middle of the pore ($z = 0$). Source numerical data are provided in source data.

The large number of cargo complex localizations outside the central pore of the NPC (>90%; Extended Data Fig. 5f,g) reflects a large accessible volume with numerous binding sites (Figs. 4c and 5c). Verification that this entire volume is accessible to rapid confined movement requires a true 3D approach, such as that reported here. The diffusion constant of the tracked M9-βGal and Imp α molecules was ~25-fold less in the vicinity of a NPC relative to free diffusion (Extended Data Fig. 6), which is an expected consequence of numerous transient binding events for the assembled cargo complexes. While we suggest that the largest contributor to the necessary binding sites on the cytoplasmic and nucleoplasmic sides of the pore are the FG repeats on extended FG polypeptides[12,43–45],

the cytoplasmic filaments and nuclear basket structure are additional probable binding site contributors[61–63]. In addition, the current data cannot rule out non-NPC binding sites, such as cytoskeletal and nucleoskeletal structures[64,65].

The described super-resolution approaches can be improved and applied in multiple ways. A third cargo imaging approach in which the NPC scaffold is labelled with a bluer blinking dye with appropriate photophysics and photon output would enable cargo transport to be imaged first at a faster frame rate without bleaching of the NPC tags, which could then be imaged second. Data quantity can be increased with alternating or parallel acquisition of the different colours. Looking beyond the NPC, these rapid 3D super-resolution strategies can be applied to address numerous cell biological questions. Trapped complexes within the rigid structural framework that generates the NPC positional stability can probably be examined with various exogenous probes and super-resolution microscopy approaches.

Online content

Any methods, additional references, Nature Research reporting summaries, source data, extended data, supplementary information, acknowledgements, peer review information; details of author contributions and competing interests; and statements of data and code availability are available at https://doi.org/10.1038/s41556-021-00815-6.

Received: 7 June 2021; Accepted: 12 November 2021;
Published online: 10 January 2022

References

1. Ribbeck, K. & Görlich, D. Kinetic analysis of translocation through nuclear pore complexes. *EMBO J.* **20**, 1320–1330 (2001).
2. Yang, W., Gelles, J. & Musser, S. M. Imaging of single-molecule translocation through nuclear pore complexes. *Proc. Natl Acad. Sci. USA* **101**, 12887–12892 (2004).
3. Kubitscheck, U. et al. Nuclear transport of single molecules: dwell times at the nuclear pore. *J. Cell Biol.* **168**, 233–243 (2005).
4. Tu, L.-C. & Musser, S. M. Single molecule studies of nucleocytoplasmic transport. *Biochim. Biophys. Acta* **1813**, 1607–1618 (2010).
5. Beck, M. & Hurt, E. The nuclear pore complex: understanding its function through structural insight. *Nat. Rev. Mol. Cell Biol.* **18**, 73–89 (2017).
6. Dickmanns, A., Kehlenbach, R. H. & Fahrenkrog, B. Nuclear pore complexes and nucleocytoplasmic transport: from structure to function to disease. *Int. Rev. Cell Mol. Biol.* **320**, 171–233 (2015).
7. Strawn, L. A., Shen, T., Shulga, N., Goldfarb, D. S. & Wente, S. R. Minimal nuclear pore complexes define FG repeat domains essential for transport. *Nat. Cell Biol.* **6**, 197–206 (2004).
8. Bayliss, R., Littlewood, T., Strawn, L. A., Wente, S. R. & Stewart, M. GLFG and FxFG nucleoporins bind to overlapping sites on importin-β. *J. Biol. Chem.* **277**, 50597–50606 (2002).
9. Allen, N. P. C., Huang, L., Burlingame, A. & Rexach, M. Proteomic analysis of nucleoporin interacting proteins. *J. Biol. Chem.* **276**, 29268–29274 (2001).
10. Fiserova, J., Richards, S. A., Wente, S. R. & Goldberg, M. W. Facilited transport and diffusion take distinct spatial routes through the nuclear pore complex. *J. Cell Sci.* **123**, 2773–2780 (2010).
11. Ma, J., Goryaynov, A. & Yang, W. Super-resolution 3D tomography of interactions and competition in the nuclear pore complex. *Nat. Struct. Mol. Biol.* **23**, 239–247 (2016).
12. Huang, K., Tagliazucchi, M., Park, S. H., Rabin, Y. & Szleifer, I. Nanocompartmentalization of the nuclear pore lumen. *Biophys. J.* **118**, 219–231 (2020).
13. Yamada, J. et al. A bimodal distribution of two distinct categories of intrinsically-disordered structures with separate functions in FG nucleoporins. *Mol. Cell. Proteom.* **9**, 2205–2224 (2010).
14. Peleg, O. & Lim, R. Y. Converging on the function of intrinsically disordered nucleoporins in the nuclear pore complex. *Biol. Chem.* **391**, 719–730 (2010).
15. Kim, S. J. et al. Integrative structure and functional anatomy of a nuclear pore complex. *Nature* **555**, 475–482 (2018).
16. Beck, M., Lucic, V., Förster, F., Baumeister, W. & Medalia, O. Snapshots of nuclear pore complexes in action captured by cryo-electron tomography. *Nature* **449**, 611–615 (2007).
17. Ma, J. & Yang, W. Three-dimensional distribution of transient interactions in the nuclear pore complex obtained from single molecule snapshots. *Proc. Natl Acad. Sci. USA* **107**, 7305–7310 (2010).
18. Maimon, T., Elad, N., Dahan, I. & Medalia, O. The human nuclear pore complex as revealed by cryo-electron tomography. *Structure* **20**, 998–1006 (2012).
19. Bui, K. H. et al. Integrated structural analysis of the human nuclear pore complex scaffold. *Cell* **155**, 1233–1243 (2013).
20. Mohr, D., Frey, S., Fischer, T., Güttler, T. & Görlich, D. Characterization of the passive permeability barrier of nuclear pore complexes. *EMBO J.* **28**, 2541–2553 (2009).
21. Timney, B. L. et al. Simple rules for passive diffusion through the nuclear pore complex. *J. Cell Biol.* **215**, 57–76 (2016).
22. Suntharalingam, M. & Wente, S. R. Peering through the pore: nuclear pore complex structure, assembly, and function. *Dev. Cell* **4**, 775–589 (2003).
23. Milles, S. et al. Plasticity of an ultrafast interaction between nucleoporins and nuclear transport receptors. *Cell* **163**, 734–745 (2015).
24. Schmidt, H. B. & Görlich, D. Transport selectivity of nuclear pores, phase separation, and membraneless organelles. *Trends Biochem. Sci.* **41**, 46–61 (2016).
25. Zahn, R. et al. A physical model describing the interaction of nuclear transport receptors with FG nucleoporin domain assemblies. *eLife* **5**, e14119 (2016).
26. Eibauer, M. et al. Structure and gating of the nuclear pore complex. *Nat. Comm.* **6**, 7532 (2015).
27. Löschberger, A. et al. Super-resolution imaging visualizes the eightfold symmetry of gp210 proteins around the nuclear pore complex and resolves the central channel with nanometer resolution. *J. Cell Sci.* **125**, 570–575 (2012).
28. Thevathasan, J. V. et al. Nuclear pores as versatile reference standards for quantitative superresolution microscopy. *Nat. Methods* **16**, 1045–1053 (2019).
29. Schlichthaerle, T. et al. Direct visualization of single nuclear pore complex proteins using genetically-encoded probes for DNA-PAINT. *Angew. Chem. Int. Ed.* **58**, 13004–13008 (2019).
30. Yoo, T. Y. & Mitchison, T. J. O-GlcNAc modification of nuclear pore complexes accelerates bidirectional transport. *J. Cell Biol.* **220**, e202010141 (2021).
31. Huang, B., Wang, W., Bates, M. & Zhuang, X. Three-dimensional super-resolution imaging by stochastic optical reconstruction microscopy. *Science* **319**, 810–813 (2008).
32. Sahl, S. J., Hell, S. W. & Jakobs, S. Fluorescence nanoscopy in cell biology. *Nat. Rev. Mol. Cell Biol.* **18**, 685–701 (2017).
33. von Diezmann, A., Shechtman, Y. & Moerner, W. E. Three-dimensional localization of single molecules for super-resolution imaing and single-particle tracking. *Chem. Rev.* **117**, 7244–7275 (2017).
34. Fridy, P. C. et al. A robust pipeline for rapid production of versatile nanobody repertoires. *Nat. Methods* **11**, 1253–1260 (2014).
35. Uno, S. et al. A spontaneously blinking fluorophore based on intramolecular spirocyclization for live-cell super-resolution imaging. *Nat. Chem.* **6**, 681–689 (2014).
36. Daigle, N. et al. Nuclear pore complexes form immobile networks and have a very low turnover in live mammalian cells. *J. Cell Biol.* **154**, 71–84 (2001).
37. Musser, S. M. & Grünwald, D. Deciphering the structure and function of nuclear pores using single-molecule fluorescence approaches. *J. Mol. Biol.* **428**, 2091–2119 (2016).
38. Chu, F.-Y., Haley, S. C. & Zidovska, A. On the origin of shape fluctuations of the cell nucleus. *Proc. Natl Acad. Sci. USA* **114**, 10338–10343 (2017).
39. Yang, W. & Musser, S. M. Nuclear import time and transport efficiency depend on importin β concentration. *J. Cell Biol.* **174**, 951–961 (2006).
40. Tu, L.-C., Fu, G., Zilman, A. & Musser, S. M. Large cargo transport by nuclear pores: implications for the spatial organization of FG-nucleoporins. *EMBO J.* **32**, 3220–3230 (2013).
41. Grossman, E., Medalia, O. & Zwerger, M. Functional architecture of the nuclear pore complex. *Annu. Rev. Biophys.* **41**, 557–584 (2012).
42. Chook, Y. M. & Blobel, G. Karyopherins and nuclear import. *Curr. Opin. Struct. Biol.* **11**, 703–715 (2001).
43. Ananth, A. N. et al. Spatial structure of disordered proteins dictates conductance and selectivity in nuclear pore complex mimics. *eLife* **7**, e31510 (2018).
44. Pulupa, J., Rachh, M., Tomasini, M. D., Mincer, J. S. & Simon, S. M. A coarse-grained computational model of the nuclear pore complex predicts Phe-Gly nucleoporin dynamics. *J. Gen. Physiol.* **149**, 951–966 (2017).
45. Fiserova, J., Spink, M., Richards, S. A., Saunter, C. & Goldberg, M. W. Entry into the nuclear pore complex is controlled by a cytoplasmic exclusion zone containing dynamic GLFG-repeat nucleoporin domains. *J. Cell Sci.* **127**, 124–136 (2014).
46. Yang, W. & Musser, S. M. Visualizing single molecules transiting through nuclear pore complexes with narrow-field epifluorescence microscopy. *Methods* **39**, 3316–3328 (2006).

47. Sun, C., Yang, W., Tu, L.-C. & Musser, S. M. Single molecule measurements of importin α/cargo complex dissociation at the nuclear pore. *Proc. Natl Acad. Sci. USA* **105**, 8613–8618 (2008).
48. Kobe, B. Autoinhibition by an internal nuclear localization signal revealed by the crystal structure of mammalian importin α. *Nat. Struct. Biol.* **6**, 388–397 (1999).
49. Lott, K. & Cingolani, G. The importin β binding domain as a master regulator of nucleocytoplasmic transport. *Biochim. Biophys. Acta* **1813**, 1578–1592 (2011).
50. Peters, R. Translocation through the nuclear pore complex: selectivity and speed by reduction-of-dimensionality. *Traffic* **6**, 421–427 (2005).
51. Schuller, A. P. et al. The cellular environment shapes the nuclear pore complex architecture. *Nature* https://doi.org//10.1038/s41586-021-03985-3 (2021).
52. Zila, V. et al. Cone-shaped HIV-1 capsids are transported through intact nuclear pores. *Cell* **184**, 1032–1046 (2021).
53. Ma, J. et al. High-resolution three-dimensional mapping of mRNA export through the nuclear pore. *Nat. Commun.* **4**, 2414 (2013).
54. Tu, L.-C., Huisman, M., Chung, Y.-C., Smith, C. S. & Grunwald, D. Deconstructing transport-distribution reconstruction in the nuclear-pore complex. *Nat. Struct. Mol. Biol.* **25**, 1061–1062 (2018).
55. Ruba, A., Kelich, J., Ma, J. & Yang, W. Reply to 'Deconstructing transport-distribution reconstruction in the nuclear-pore complex'. *Nat. Struct. Mol. Biol.* **25**, 1061–1064 (2018).
56. Onischenko, E. et al. Natively unfolded FG repeats stabilize the structure of the nuclear pore complex. *Cell* **171**, 904–917.e19 (2017).
57. Rout, M. P., Aitchison, J. D., Magnasco, M. O. & Chait, B. T. Virtual gating and nuclear transport: the hole picture. *Trends Cell Biol.* **13**, 622–628 (2003).
58. Frey, S., Richter, R. P. & Görlich, D. FG-rich repeats of nuclear pore proteins form a three-dimensional meshwork with hydrogel-like properties. *Science* **314**, 815–817 (2006).
59. Lim, R. Y. H. et al. Nanomechanical basis of selective gating by the nuclear pore complex. *Science* **318**, 640–643 (2007).
60. Kapinos, L. E., Schoch, R. L., Wagner, R. S., Schleicher, K. D. & Lim, R. Y. M. Karyophein-centric control of nuclear pores based on molecular occupancy and kinetic analysis of multivalent binding with FG nucleoporins. *Biophys. J.* **106**, 1751–1762 (2014).
61. Strambio-de-Castillia, C., Niepel, M. & Rout, M. P. The nuclear pore complex: bridging nuclear transport and gene regulation. *Nat. Rev. Mol. Cell Biol.* **11**, 490–501 (2010).
62. Walther, T. C. et al. The cytoplasmic filaments of the nuclear pore complex are dispensable for selective nuclear protein import. *J. Cell Biol.* **158**, 63–77 (2002).
63. Ben-Efraim, I., Frosst, P. D. & Gerace, L. Karyopherin binding interactions and nuclear import mechanism of nuclear pore complex protein Tpr. *BMC Cell Biol.* **10**, 74 (2009).
64. Goldberg, M. W. Nuclear pore complex tethers to the cytoskeleton. *Semin. Cell Dev. Biol.* **68**, 52–58 (2017).
65. Simon, D. N. & Wilson, K. L. The nucleoskeleton as a genome-associated dynamic 'network of networks'. *Nat. Rev. Mol. Cell Biol.* **12**, 695–708 (2011).
66. Ovesný, M., Křížek, P., Borkovec, J., Švindrych, Z. & Hagen, G. M. ThunderSTORM: a comprehensive ImageJ plugin for PALM and STORM data analysis and super-resolution imaging. *Bioinformatics* **30**, 2389–2390 (2014).
67. von Appen, A. et al. In situ structural analysis of the human nuclear pore complex. *Nature* **526**, 140–143 (2015).

Methods

A step-by-step protocol describing the 3D microscopy imaging method reported in this paper is provided at *Protocol Exchange*[68].

Experimental methods. *Protein mutation, expression and purification.* The expression and purification of RanGDP (refs. [40,69–71]), NTF2 (refs. [71,72]), transportin[73], M9-βGal-8C (ref. [40]) and a mutated version of the anti-GFP nanobody LaG-9 (ref. [34]) largely followed the approaches in the indicated work. A carboxy-terminal cysteine on the LaG-9 nanobody was generated by mutation (S151C) using the QuikChange protocol (Agilent Technologies) to produce plasmid pET21b-LaG9(S151C). Plasmid pNLS-2×BFP(4C), which encodes NLS-2×BFP(4C), was created by a Y66H mutation[74] in each of the GFP genes of pNLS-2×GFP(4C)[46] via the QuikChange method. For simplicity, the M9-βGal-8C and NLS-2×BFP(4C) proteins are referred to as M9-βGal and NLS-2xBFP, respectively, throughout this paper. All plasmids were confirmed by DNA sequencing. Plasmids pM9-βGal-8C, pET21b-LaG9(S151C) and pNLS-2×BFP(4C) are available from Addgene (172489, 172490 and 176151, respectively). For clarity, descriptions of all protein expressions and purifications are provided below. When used, antibiotics were 50 μg ml^{-1} for ampicillin (Amp) and 30 μg ml^{-1} for kanamycin (Kan). All purified proteins were stored at −80 °C until use.

RanGDP. BL21(DE3) cells transfected with pQE32-Ran[70] were inoculated into 5 ml of LB medium with 2% glucose and Amp, and cultured overnight at 37 °C. The following day, the starter culture was transferred to 1 litre of LB medium with 2% glucose and Amp, grown at 37 °C until an OD_{600} of ~0.8, induced with 1 mM isopropyl β-D-1-thiogalactopyranoside (IPTG) and grown for another 4 h at 27 °C before pelleting the culture (4,000×*g*, 20 min, 4 °C). Cells were resuspended in 20 ml of 20 mM potassium phosphate (K-Phos), 200 mM NaCl, 0.5 mM $MgCl_2$, 10 mM imidazole, 4 mM β-mercaptoethanol (βME), pH 7, and protease inhibitors (PIs; 10 mM phenylmethane sulfonyl fluoride, 100 μg ml^{-1} trypsin inhibitor, 20 μg ml^{-1} leupeptin and 100 μg ml^{-1} pepstatin), and lysed by French press (three times at 16,000 psi). The lysate was centrifuged (15,000×*g*, 20 min, 4 °C), and the supernatant was mixed with 0.5 ml Ni-NTA resin. After incubation for 30 min at 4 °C, the suspension was transferred to a gravity column. The resin was washed with 15 ml of 20 mM K-Phos, 500 mM NaCl, 0.5 mM $MgCl_2$, 20 mM imidazole, 0.1% Triton X-100, pH 7.0, and PIs and then 15 ml of 20 mM K-Phos, 50 mM NaCl, 0.5 mM $MgCl_2$, 20 mM imidazole, pH 8. Fractions (1 ml) were eluted with 20 mM K-Phos, 50 mM NaCl, 0.5 mM $MgCl_2$ and 250 mM imidazole, pH 8. Major elution fractions were combined and then subjected to cation-exchange chromatography in 20 mM K-Phos, 50 mM NaCl, 0.5 mM $MgCl_2$, pH 8 using a MonoS column (GE Pharmacia Biotech, 17-0547-01) and a linear NaCl gradient (with 500 mM NaCl in the second buffer) to separate RanGDP (first peak at ~150 mM NaCl) from RanGTP (second peak at ~250 mM NaCl).

NTF2. BL21(DE3) cells transfected with pET15b-NTF2 (ref. [75]) were inoculated into 5 ml of LB medium and Amp, and incubated at 37 °C overnight. This starter culture was transferred to 2 litres of LB medium and Amp, grown at 37 °C for ~5 h (until OD_{600} of ~0.8), and then grown for an additional 4 h at 27 °C after inducing with 1 mM IPTG. Cells were resuspended in 20 ml of 20 mM Tris, 200 mM NaCl, 5 mM $MgCl_2$, 10 mM imidazole, pH 8.0, and PIs, and then lysed as was done for the purification of Ran. NTF2 was precipitated from the cleared lysate with saturated ammonium sulfate (at ~40–50% saturation), and recovered by centrifugation (4,000×*g*, 20 min, 4 °C). The pellet was dissolved in 5 ml of 50 mM Tris, pH 8, over 1 h. The NTF2 solution was then purified using a HiPrep Q FF anion-exchange resin column (GE Healthcare Bioscience, 17-5190-01) with the dissolution buffer and a linear NaCl gradient, followed by Superdex 75 size-exclusion chromatography (GE Healthcare Bioscience, 17-5174-01) in the dissolution buffer.

Transportin. BL21-Gold(DE3) cells transfected with pGEX4TT3-TEV-KapBeta2 (ref. [73]) were inoculated into 20 ml of LB medium and Amp, and grown overnight at 37 °C. The starter culture was transferred to 2 litres of LB medium and Amp, grown to an OD_{600} of ~0.6 at 25 °C, and then induced with 0.5 mM IPTG for 12 h at 25 °C. The cells were resuspended in 15 ml of transportin lysis buffer (50 mM HEPES buffer, 150 mM NaCl, 15% glycerol, 2 mM dithiothreitol (DTT), 2 mM EDTA, pH 7.4 and PIs) per litre of original culture, and then lysed as was done during for the purification of Ran. The cleared lysate was mixed with 500 μl glutathione sepharose resin (GE Healthcare, 17-0756-01) and loaded onto a gravity column, which was washed with 20 ml of transportin lysis buffer, 25 ml of 50 mM HEPES, 100 mM NaCl, 1 mM EGTA, 10 mM magnesium acetate, 2 mM DTT, 15% glycerol, 5 mM ATP, pH 7.4, and PIs, and 25 ml of 20 mM HEPES, 20 mM NaCl, 2 mM EDTA, 10% glycerol, 2 mM DTT, pH 7.4. The GST tag was cleaved by incubating the sepharose resin with 20 mM HEPES, 20 mM NaCl, 2 mM EDTA, 10% glycerol, 2 mM DTT, 0.5 units μl^{-1} TEV protease (ThermoFisher Scientific, 12575015), pH 7.4 for 2 h at room temperature, and the solution was then collected (0.5 ml fractions). The transportin protein was further purified by Enrich Sec 650 size-exclusion chromatography (Bio-Rad, 7801650) in 20 mM HEPES, 110 potassium acetate, 5 mM sodium acetate, 2 mM magnesium acetate and 2 mM DTT, pH 7.4.

M9-βGal. BL21(DE3) cells transfected with pET30a-M9-βGal-8C (ref. [40]) were inoculated into 4 ml of LB medium and Kan, and cultured overnight at 37 °C. The starter culture was transferred into 1 litres of LB medium and Kan, grown at 37 °C for 2–3 h (until OD_{600} of ~0.8), and then induced overnight at 22 °C with 0.15 mM IPTG. The cells were resuspended in 15 ml of 5 mM Tris, 500 mM NaCl, 5 mM $MgCl_2$, 4 mM βME, 10% glycerol, pH 8.0, and PIs and a pinch of DNase I, and then lysed as was done for the purification of Ran. The cleared lysate was incubated with 0.5 ml Ni-NTA resin for 30 min at 4 °C, and the suspension was then transferred to a gravity column. The resin was washed with 15 ml of 5 mM Tris, 500 mM NaCl, 5 mM $MgCl_2$, 4 mM βME, 0.1% Triton X-100, pH 8, and then 15 ml of 5 mM Tris, 100 mM NaCl, 10 mM imidazole, pH 8. Fractions (0.5 ml) were eluted with 5 mM Tris, 100 mM NaCl, 250 mM imidazole, pH 8. The most concentrated fraction was further purified by Enrich Sec 650 size-exclusion chromatography using 20 mM HEPES and 150 mM NaCl, pH 7.3.

LaG-9(S151C). BL21(DE3) cells transfected with pET21b-LaG9(S151C) were inoculated into 5 ml of LB medium and Amp, and cultured overnight at 37 °C. The starter culture was transferred into 1 litres of LB medium and Amp, which was grown at 37 °C until the OD_{600} was ~0.8, and then induced with 0.1 mM IPTG for 20 h at 20 °C. The cells were resuspended in 10 ml ice-cold 20 mM Tris, 0.5 mM EDTA, 500 mM sucrose, 10 mM βME, 0.3 mM $MgSO_4$, pH 8.0, and PIs, and then lysed as was done for the purification of Ran. The cleared lysate was incubated with 0.5 ml Ni-NTA resin for 30 min at 4 °C, and the suspension was then transferred to a gravity column. The resin was washed with 15 ml of 20 mM Tris, 900 mM NaCl, 10 mM βME, 0.1% Triton X-100, pH 8.0, and then 15 ml of 20 mM Tris, 150 mM NaCl, 10 mM imidazole, pH 8.0. Fractions (0.5 ml) were eluted with 20 mM Tris, 150 mM NaCl, 250 mM imidazole, pH 8.0. The most concentrated fraction was further purified by Superdex 75 size-exclusion chromatography (GE Healthcare Bioscience, 17-5174-01) using 20 mM HEPES and 150 mM NaCl, pH 7.3.

Imp α. BL21(DE3) cells transfected with pRSET-hSRPα (ref. [76]) were inoculated into 5 ml of LB medium and Amp, and cultured overnight at 30 °C. The starter culture was then transferred into 2 litres of LB medium and Amp, grown at 37 °C until the OD_{600} was ~0.8, and then induced with 0.8 mM IPTG for 4.5 h at 28 °C. The cells were resuspended in 10 ml of 20 mM Tris, 200 mM NaCl, 5 mM $MgSO_4$, 10 mM imidazole, 4 mM βME, pH 8.0, and PIs, and then lysed as was done for the purification of Ran. The cleared lysate was incubated with 0.6 ml Ni-NTA resin for 30 min at 4 °C, and the suspension was then transferred to a gravity column. Next, the resin was washed with 20 ml of 20 mM Tris, 1 M NaCl, 5 mM $MgSO_4$, 10 mM imidazole, 4 mM βME, 0.1% TX-100, pH 8.0 and PIs, and then 20 ml of 20 mM Tris, 100 mM NaCl, 10 mM imidazole, pH 8. Fractions (0.5 ml) were eluted with 20 mM Tris, 100 mM NaCl, 250 mM imidazole, pH 8.0. The most concentrated fraction was further purified by Superdex 200 size-exclusion chromatography (GE Healthcare Bioscience, 28-9909-44) using 20 mM HEPES and 150 mM NaCl, pH 7.3.

Imp β. BL21(DE3) cells transfected with pQE9-Imp β (ref. [69]) were inoculated into 5 ml of LB medium with 2% glucose and Amp, and cultured overnight at 37 °C. The starter culture was then transferred into 1 litre of LB medium with 2% glucose and Amp, grown at 37 °C until the OD_{600} was ~0.8, and then induced with 0.7 mM IPTG for 3 h at 37 °C. The cells were resuspended in 6 ml of 5 mM Tris, 500 mM NaCl, 5 mM $MgSO_4$, 10 mM imidazole, 4 mM βME, pH 8.0, and PIs, and then lysed as was done for the purification of Ran. The cleared lysate was incubated with 0.5 ml Ni-NTA resin for 30 min at 4 °C, and the suspension was then transferred to a gravity column. The resin was washed with 20 ml of 5 mM Tris, 500 mM NaCl, 5 mM $MgSO_4$, 10 mM imidazole, 4 mM βME, 0.1% Triton X-100, pH 8.0, and PIs, and then 20 ml of 5 mM Tris, 100 mM NaCl, 10 mM imidazole, pH 8. Fractions (0.5 ml) were eluted with 5 mM Tris, 100 mM NaCl, 250 mM imidazole, pH 8.0. The most concentrated fraction was further purified by Superdex 200 size-exclusion chromatography using 20 mM HEPES, 110 mM potassium acetate, 5 mM sodium acetate, 2 mM magnesium acetate and 2 mM DTT, pH 7.4.

NLS-2×BFP. JM109 cells transfected with pNLS-2×BFP(4C) were inoculated into 5 ml of LB medium and Amp, and cultured overnight at 37 °C. The starter culture was then transferred into 1 litre of LB medium and Amp, grown at 37 °C until the OD_{600} was ~0.8, and then induced with 0.7 mM IPTG for 14 h at 25 °C. The cells were resuspended in 6 ml of 5 mM Tris, 500 mM NaCl, 5 mM $MgSO_4$, 10 mM imidazole, 4 mM βME, pH 8.0, and PIs, and then lysed as was done for the purification of Ran. The cleared lysate was incubated with 0.5 ml Ni-NTA resin for 30 min at 4 °C, and the suspension was then transferred to a gravity column. The resin was washed with 20 ml of 5 mM Tris, 500 mM NaCl, 5 mM $MgSO_4$, 10 mM imidazole, 4 mM βME, 0.1% Triton X-100, pH 8.0, and PIs, and then 20 ml of 5 mM Tris, 100 mM NaCl, 10 mM imidazole, pH 8.0. Fractions (0.5 ml) were eluted with 5 mM Tris, 100 mM NaCl, 250 mM imidazole, pH 8.0. The most concentrated protein fraction was further purified by Superdex 200 size-exclusion chromatography using 20 mM HEPES, 110 mM potassium acetate, 5 mM sodium acetate, 2 mM magnesium acetate and 2 mM DTT, pH 7.4.

Protein labelling. The spontaneously blinking dye HMSiR[35] (SaraFluor 650B-maleimide; Goryo Chemical, A209-01) or Alexa568 (ThermoFisher Scientific,

A20341) was attached to the C-terminal cysteine on LaG-9(S151C) by incubating it with a 15-fold molar excess of the maleimide derivative of the dyes dissolved in dimethylsulfoxide (DMSO) at room temperature for 15 min. Excess dye was removed by adding the dye–protein mixture to 0.1 ml Ni-NTA resin (30 min incubation), washing the resin-bound protein with 20 ml of 20 mM HEPES, 500 mM NaCl, 0.1% Triton X-100, 4 mM βME, pH 7.3, and then eluting the labelled nanobody with 20 mM HEPES, 150 mM NaCl and 250 mM imidazole, pH 7.3.

The eight surface cysteine residues on M9-βGal were labelled with Atto542 maleimide (Atto-Tec, AD 542) using a 150-fold molar excess of dye dissolved in DMSO. To label the four surface cysteines on Imp α, a 70-fold molar excess of Atto542 maleimide was used. Excess dye was removed by adding the dye–protein mixture to 0.1 ml Ni-NTA resin (30 min incubation), washing the resin-bound protein with 5 ml of 20 mM HEPES, 150 mM NaCl, 0.1% Triton X-100, 4 mM βME, pH 7.3, and eluting with 20 mM HEPES, 150 mM NaCl and 250 mM imidazole, pH 7.3.

Protein concentrations. Protein concentrations were determined on the basis of the densitometry of bands on SDS–PAGE gels stained with Coomassie Blue R-250 using BSA as a standard and a ChemiDoc MP imaging system (Bio-Rad). The purity of dye-labelled proteins was assayed by direct in-gel fluorescence imaging using the same ChemiDoc imaging system, and was established as >95%.

Cell culture. U-2 OS-CRISPR-NUP96-mEGFP clone 195 (300174, CLS) and U-2 OS cells (300364, CLS)[28] were obtained in January 2020 and were used without authentication. Cells were grown in McCoy's 5A (modified) medium (ThermoFisher Scientific, 16600082) supplemented with 100 U ml^{-1} penicillin–streptomycin (ThermoFisher Scientific, 15140148), 1 mM sodium pyruvate (ThermoFisher Scientific, 11360070), 1× MEM non-essential amino acids solution (ThermoFisher Scientific, 11140050) and 10% (v/v) fetal bovine serum (ThermoFisher Scientific, A3160401) in 5% (v/v) CO_2 enriched air at 37 °C. Cells were typically grown to ~95% confluency, were split using Accutase (ThermoFisher Scientific, A1110501) and were tested every month for mycoplasma contamination (InvivoGen, rep-pt1). For microscopy experiments, freshly split cells were grown overnight (<3% confluence) on coverslips pre-treated with 0.01% poly-L-lysine (Sigma, P4832) for 5 min, which reduced cell detachment after permeabilization.

Single-molecule transport experiments. Flow chambers (~10 µl) were constructed by inverting a small coverslip (10.5×35 mm; Electron Microscopy Sciences, 72191-35) with beads of high-vacuum grease parallel to its short edges over a no.1.5 coverslip (24×60 mm; VWR, 16004-312) on which U-2 OS cells were grown overnight. Cells were permeabilized by incubating with 40 µg ml^{-1} digitonin in import buffer (IB; 20 mM HEPES, 110 mM potassium acetate, 5 mM sodium acetate, 2 mM magnesium acetate and 1 mM EGTA, pH 7.3) for 2 min. Permeabilized cells were washed once with 10 µl IB containing 1.2% (w/v) polyvinylpyrrolidone (PVP; 360,000 g mol^{-1}; Sigma, P5288)[2]. Then, 10 µl of 100 nM nanobody-HMSiR in IB + 1.2% PVP (IB-PVP) was flowed onto the permeabilized cells and incubated for 3 min. The cells were washed twice (2×10 µl) with IB-PVP. The cells were then ready for single-molecule nuclear transport experiments. The LaG9(S151C) nanobody showed high specificity towards the mEGFP domain in U-2 OS-CRISPR-NUP96-mEGFP cells (Extended Data Fig. 1a and Supplementary Video 1).

For approach 1, the transport mix consisting of 0.5 µM RanGDP, 1 µM NTF2, 1 mM GTP, 1 µM transportin and 1 nM M9-βGal(Atto542) in IB-PVP was added to the permeabilized nanobody-tagged cells. As it takes ~1 min for the Ran concentration at the NE to become established and reach steady-state[39], this time was used to find the bottom surface of the cell and prepare for image acquisition. Approximately 2 min was used for imaging cargo transport (3 ms frame^{-1}, 30 movies, each comprising 1,000 frames), and ~8 min for acquiring nanobody localizations (50 ms frame^{-1}, 14 movies, each comprising 500 frames with a 5-s gap between movies).

For approach 2, the transport mix consisted of 1.5 µM RanGDP, 1 µM NTF2, 1 mM GTP, 0.5 µM Imp β, 0.5 µM NLS-2×BFP and 1 nM Imp α(Atto542) in IB-PVP. In the first ~8 min, nanobody localizations were acquired (50 ms frame^{-1}, 14 movies, each comprising 500 frames with a 5 s gap between movies). Then, the next ~2 min was used to image cargo complexes (2 ms frame^{-1}, 50 movies, each comprising 1,000 frames). The first two to three movies were not included in the analysis because of the substantial background fluorescence from already transported cargo complexes. After this time, sufficient photobleaching had occurred, which allowed for single-particle detection.

2D microscopy for bulk transport. Bulk import of M9-βGal(Atto542) and Imp α(Atto542) (Extended Data Fig. 4) was measured using wide-field fluorescence with a Nikon Eclipse Ti equipped with an ×100 oil-immersion objective (Nikon Apo TIRF, 1.49 NA). Epifluorescence excitation from a white-light lamp (532 ± 5 nm) was selected (Chroma zet532/×10, zt532rdc-UF2, and ET550LP), and emission was recorded using a Prime 95B camera. For these assays, the permeabilized cells were washed twice with IB-PVP before adding transport mix.

3D super-resolution microscopy. The core of our 3D microscope set-up (Fig. 1a) was a Zeiss Axiovert 200M equipped with an ×100 oil-immersion objective (Zeiss Alpha Plan-Apochromat, 1.40 NA) on a vibration isolation table. A nearly flat sample plane illumination was obtained with a πShaper (Edmund Optics, 12-644) using diode lasers (0.7–0.8 mm initial diameter; 488, 532 and 647 nm with 400, 300 and 120 mW maximum power, respectively) directed through the epifluorescence excitation path from which all manufacturer-installed optics before the dichroic mirror were removed, except for the tube lens. The flattened beam profiles exiting the πShaper were compressed seven times and converted to circularly polarized light with half ($\lambda/2$) and a quarter ($\lambda/4$) waveplates (Newport, 10RP42-1 and 10RP44-1) before entering the microscope as a slightly converging illumination beam. A self-configured AO system (Imagine Optic, MicAO) was incorporated into the emission path between the microscope and the EMCCD camera (Photometrics Evolve 128 Delta). A 400-mm focal length tube lens (L1; Thorlabs, TL400-A) increased the diameter of the objective exit pupil (~5 mm) to ~12 mm, which was directed by a mirror to the centre of an ~15 mm diameter deformable mirror (DM; Imagine Optic, Mirao 52-e). Considering the 165-mm focal length of the microscope tube lens, this represents an exit pupil magnification of ~2.42. A second lens, L2 (identical to L1), re-created the sample image with the wavefront corrected by the DM. A ×2 lens magnifier (Edmund Optics, 54-356) was used to magnify the image ~2-fold. Image magnification was determined using a calibration slide (Amscope, MR095) and yielded 118-nm square pixels. A flip mirror (FM) diverted the beam from the DM to a Shack–Hartman wavefront sensor (WFS; Imagine Optic, HASO4), which was positioned in a conjugate plane to the DM after a 100-mm focal length tube lens (L3; Thorlabs, TL100-A), which compressed the pupil diameter four times to ~3 mm. All introduced lenses were chromatically corrected. An Optosplit III (Cairn Research) was incorporated before the camera to enable simultaneous multicolour imaging, although this option was not used here due to the different imaging timescales for the two colours. Both green and red emission channels were collected with a double-bandpass filter set (Chroma, ZT532/640/NIR-RPC-UF2 and zet532/640m). A self-configured TIRF-Lock system (Mad City Labs) installed using an infrared (IR) laser (850 nm, 20 mW; Thorlabs, LDM850) provided a z stability for the coverslip of <3 nm for the duration of the experiment. This system measures the deflection of the total internally reflected IR laser beam focused with a 50 mm lens (L4; Edmund Optics, 88-724) on a quadrant detector, which then enables z-positional correction of the coverslip via a feedback loop with a z nanostage. Microscope coverslips were mounted within a home-built aluminium frame and held in place with high-vacuum grease. The mounted coverslip was suspended within the piezo-stage (Mad City Labs, Nano-LPS200) opening with a manufacturer provided scaffold, and covered with a glass plate during acquisition to reduce air current drift. The AO system was used to correct the aberrations introduced by the microscope imaging optics using two approaches enabled by software provided by the manufacturer (Imagine Optic). First, the emission from a 1-µm fluorescent bead (ThermoFisher Scientific, T7282) embedded in 2% agarose (Sigma Aldrich, A7174) was directed to the WFS. The shape of the DM was then altered in an iterative process to achieve a substantially flattened wavefront. Next, the emission beam from a diffraction-limited 0.1-µm bead (ThermoFisher Scientific, T7279) embedded in 2% agarose was directed to the camera, and the DM was adjusted to achieve the highest quality image using an iterative algorithm based on an intensity-based merit factor[77]. This second correction has the advantage that it utilized the exact optical path used for eventual imaging, unlike the first approach, in which the beam was diverted to the WFS. When satisfied with the corrected point spread function (PSF), 60 nm root mean square (r.m.s.) astigmatism was added to generate the z-dependent spot ellipticity needed for 3D information[31]. The microscope was then ready for imaging. This two-step correction was always done in the red channel, and the optimized shape of the DM obtained for the red channel was also used as the primary correction for the green channel. However, when acquiring movies in the green channel, a 30 nm r.m.s. defocus was additionally applied, which made the z foci of the green and red channels very close (within ~30 nm). Immediately after imaging cargo transport and obtaining NPC localizations, z-stack image sequences (100 ms frame^{-1}, 41 steps, step size of 25 nm) from five different 0.1-µm beads embedded in 2% agarose were obtained in both green and red channels to generate 3D calibration curves[31] (Fig. 1d). Image sequences (100 frames, 50 ms frame^{-1}) were also acquired to calculate the image alignment matrix between the two imaging channels.

3D diffusion constant. The diffusion constant for isotropic motion in three dimensions can be estimated using a step-size probability distribution. In one dimension, the step sizes follow a Gaussian (normal) distribution[78]. Assuming all jump distances are positive (to more readily compare with 2D and 3D cases), the normalized 1D step size probability distribution is as follows:

$$p(x,t)\mathrm{d}x = \frac{2b}{\sqrt{4\pi Dt}} \exp\left(-\frac{x^2}{4Dt}\right)\mathrm{d}x \quad (1)$$

where D is the translational diffusion constant, t is the camera integration time, b is the bin size, and the factor of 2 accounts for the fact that the data are plotted using $|x|$. The 2D step size probability distribution is as follows:

$$p(r,t)\mathrm{d}r = \frac{1}{\sqrt{4\pi Dt}}\exp\left(-\frac{x^2}{4Dt}\right)\frac{1}{\sqrt{4\pi Dt}}\exp\left(-\frac{y^2}{4Dt}\right)2\pi r\mathrm{d}r = \frac{br}{2Dt}\exp\left(-\frac{r^2}{4Dt}\right)\mathrm{d}r \quad (2)$$

where $r^2 = x^2 + y^2$, $2\pi r\mathrm{d}r$ is the volume element for a circle, and the bin size is included[79]. Similarly, the 3D step size probability distribution is as follows:

$$p\,(r,\,t)\,\mathrm{d}R = \frac{1}{\sqrt{4\pi Dt}}\exp\left(-\frac{x^2}{4Dt}\right)\frac{1}{\sqrt{4\pi Dt}}\exp\left(-\frac{y^2}{4Dt}\right)\frac{1}{\sqrt{4\pi Dt}}\exp\left(-\frac{z^2}{4Dt}\right)4\pi R^2\mathrm{d}R = \frac{bR^2}{\sqrt{4\pi}(Dt)^{3/2}}\exp\left(-\frac{R^2}{4Dt}\right)\mathrm{d}R \quad (3)$$

where $R^2 = x^2 + y^2 + z^2$, $4\pi R^2\mathrm{d}R$ is the volume element for the surface of a sphere, and the bin size is included. Assuming three distinct molecular populations with different diffusion constants,

$$p(r,t)\mathrm{d}R = \frac{bR^2}{\sqrt{4\pi}}\left[\frac{\mathrm{A}}{(D_1t)^{3/2}}\exp\left(-\frac{R^2}{4D_1t}\right) + \frac{\mathrm{B}}{(D_2t)^{3/2}}\exp\left(-\frac{R^2}{4D_2t}\right) + \frac{(1-\mathrm{A}-\mathrm{B})}{(D_3t)^{3/2}}\exp\left(-\frac{R^2}{4D_3t}\right)\right]\mathrm{d}R \quad (4)$$

where A, B and $1 - A - B$ are weighting factors for the three distributions.

Computational methods. *Software.* The Nikon microscope was controlled by NIS-Elements AR 5.02.01 (Nikon Instruments). The Zeiss microscope was controlled by Metamorph 7.7.7 (Molecular Devices). The DM and WFS were controlled by MicAO 1.3 and CasAO 1.0, respectively (Imagine Optic). The TIRF-lock system was controlled by a standalone LabVIEW 2015 program (National Instruments) provided by Mad City Labs. Data were visualized, analysed and plotted using ImageJ (Fiji 1.52P), Origin 8.5 (OriginLab), Kaleidagraph 4.5.2 (Synergy Software), Microsoft Excel 16.16.20 (200307) (Microsoft) and SnapGene 5.3.2 (GSL Biotech). With the exception of the simulations and the initial determination of 3D coordinates, all data were analysed with programs written in Matlab R2018a (Mathworks), which are summarized in Supplementary Table 1.

Simulations. Two different types of simulations were used to guide the analyses and assist with the interpretation of the results, both of which used Microsoft Excel. Supplementary Data 1 (software file 1) models the random appearance in 3D of fluorescent spots from labelled NUP96 molecules based on coordinates from the electron microscopy density map of the human NPC[67]. The centroid of the localizations was assumed to be located at the C terminus of NUP96. Although the position of the dye labels relative to this density map are not known, they are within ~6–7 nm of the labelled site (Fig. 2b). Options are included that allow the localization precision to be either static (fixed) or experimentally determined z-dependent values. The model NPC scaffold can be stochastically rotated, translated or tilted from the z axis to encompass the range of possibilities for localized structures within the NE. For rotations and translations, values were randomly selected from a linear distribution function. For tilts and static localization precision analyses, values were randomly selected from normal distributions defined by the provided standard deviation (mean = 0). For each localization, a photon count was randomly selected from a log-normal distribution with scale and shape parameters determined from experimental measurements (Extended Data Fig. 2f). The photon count was used to generate the z-dependent localization precision of the spot, as defined by experimentally determined fit curves (Fig. 1f). Since Supplementary Data 1 (software file 1) generates average precision values over input z and photon ranges, it was used to estimate average experimental single-particle precision values.

Supplementary Data 2 (software file 2) models the random appearance of fluorescence spots appearing in the cytoplasmic and nucleoplasmic compartments and within the NPC central pore. This is a coarse simulation of the experimental model as it does not include detailed structural information for the NPC or dynamic information on particle trajectories, which could have notable effects on spatial densities. The intention of this simulation was to verify that localizations within the NE region could arise from the localization error (Extended Data Fig. 5e). The z-dependent localization precision values were generated as in Supplementary Data 1 (software file 1). Spot densities in the various regions are variable parameters, as are the annular diameter and width of the central channel localizations.

Major errors in resolving the NPC scaffold. Using the experimental data as a guide, limits on important errors in resolving the NPC scaffold were obtained through simulations [Supplementary Data 1 (software file 1)], and are summarized in Fig. 3. While particle localization precision values are the largest individual errors in resolving the NPC scaffold in our current imaging strategy, the largest potential sources of additional important errors are biological movements (natural fluctuations in NPC location either due to moment of the NE or NPC movement within the NE). Instrument stability errors (for example, movements of the sample holder) are assumed to be subsumed into the localization errors. All of the cartesian (x, y and z) movements are collectively referred to as the 'jiggle', and the only angular movement considered is the tilt of the cylindrical scaffold from the normal to the NE. We have not taken into account the error in the rotational alignment of clusters (that is, we assumed that all clusters are perfectly aligned); the parameters used here for error comparisons are largely independent of this rotational alignment due to the small tilt angles. The radial distribution histograms were fit with a Gaussian function, $y = A \times \exp[-(r-\mu_r)^2/2\sigma_{rw}^2]$, and the z height histograms were fit with a symmetric double Gaussian centred on the origin, $y = B \times \{\exp[-(z-\mu_z)^2/2\sigma_{zw}^2] + \exp[-(z+\mu)^2/2\sigma_{zw}^2]\}$. Average (±s.d.) radial and z widths were determined for various tilt and jiggle values from 20 independent simulations of ~2,300–2,400 localizations (reduced from 2,500 by z selection), a fixed cluster size of 13 and a z centroid of 0 ± 200 nm (to model the variable precision in the experiments).

Spot identification and 3D localization. All image sequences were analysed using Fiji[80] with the Thunderstorm[66] plug-in. The maximum likelihood method was used for all single-molecule localizations, yielding spot centroids (x and y positions) and widths in x and y. The z coordinates were obtained from calibration curves obtained with 0.1-µm beads, and were fit as previously described[31] for display purposes (Fig. 1d,e) or as implemented by ThunderStorm[66] for image analysis. For pore localization data, two post-processing options were used: 'remove duplicates' (which eliminates overlapping molecules) and 'density filters' (which eliminates most spots between NPC clusters).

Alignment of the green (Atto542) and red (HMSiR) channels. The accurate alignment of images in distinct colour channels is essential to any super-resolution multicolour imaging scheme. Chromatic aberration is a common alignment issue since different wavelengths are focused at different spots along the optical axis. While we were careful to choose lenses designed to reduce these effects, chromatic mis-matches still remained and introduced errors in nanometre-scale precision estimates. The AO system was a major advantage here, as it was used to roughly align the z focus of the two channels. Fine tuning of the z position was obtained through use of distinct z-calibration curves for the two colour channels. We have used the red channel (NUP96 localizations) as the reference, and corrected the green channel (cargo localizations) coordinates to the red channel coordinate system. This was accomplished by applying two successive corrections to the green channel coordinates, first to x and y and then to z.

Image alignment in x and y. To determine the alignment matrix between the two imaging channels, five different 0.1-µm beads were successively imaged in the red and green channels without changing the DM settings (100 frames each; 50 ms frame^{-1}), and the mean x and y positions for each bead were determined. The alignment matrix to transform the x and y green channel coordinates into red channel coordinates was obtained as previously described[81] using rotational and translational corrections. This process was repeated for each nucleus using images collected immediately after the NPC localization measurements. The standard deviation of the differences between the transformed green channel coordinates and the red channel coordinates was considered the alignment precision in x and y ($\sigma_{a,x}$ and $\sigma_{a,y}$), and was typically ~0.1–2 nm for both x and y.

Image alignment in z. From repeated experiments, it became apparent that the green and red emission foci differed by ~100 nm. However, since the two-step AO PSF corrections were performed for each experiment, there was variation in the distance between the foci. Thus, an ~100 nm correction was introduced with the DM by applying a 30 nm r.m.s. defocus when switching from the red channel to the green channel to more closely position the green and red emission foci. The 30 nm r.m.s. defocus was removed when switching back to the red channel. The remaining correction needed for each experiment was obtained by measuring the mean z position for five 0.1-µm beads in each channel (± the 30 nm r.m.s. defocus as appropriate) to accurately determine the distance between the green and red z-calibration curves. With these independent channel calibrations, the standard deviation of the difference between the five mean z-position measurements was ~3–7 nm, which was considered to be the z-alignment precision ($\sigma_{a,z}$).

Precision. The precision in x, y and z was determined as the standard deviation of the measured position over 100 images of 0.1-µm beads embedded in 2% agarose. Precision was measured at various z positions for various excitation intensities and integration times. The z-dependent precision values in x, y and z were fit using the following equations (Fig. 1f):

$$\sigma_{p,x} = g_1\sqrt{1 + \left(\frac{(z-g_2)}{g_3}\right)^2 + g_4\left(\frac{(z-g_2)}{g_3}\right)^4} \quad (5)$$

$$\sigma_{p,y} = g_5\sqrt{1 + \left(\frac{(z-g_6)}{g_7}\right)^2 + g_8\left(\frac{(z-g_6)}{g_7}\right)^4} \quad (6)$$

$$\sigma_{p,z} = g_9\sqrt{\sigma_{p,x}^2 + \sigma_{p,y}^2} \quad (7a)$$

$$\sigma'_{p,z} = g_9 \sqrt{\begin{array}{l} g_1^2\left(1+\left(\frac{(z-g_2-g_{10})}{g_3}\right)^2+g_4\left(\frac{(z-g_2-g_{10})}{g_3}\right)^4\right) \\ +g_5^2\left(1+\left(\frac{(z-g_6-g_{10})}{g_7}\right)^2+g_8\left(\frac{(z-g_6-g_{10})}{g_7}\right)^4\right) \end{array}} \quad (7b)$$

where g_1 to g_{10} are fit constants, whose experimentally determined values (Fig. 1f) are used in Supplementary Data 1 (software file 1) and Supplementary Data 2 (software file 2). Equations (5) and (6) were modified from Huang et al.[31]. Equation (7b) is identical to equation (7a), except for the minor shift in the minimum provided by g_{10}. To compare values obtained under different conditions, all experimental precision values were normalized to 3,000 photons by multiplying the measured precision by $(N_p/3{,}000)^{1/2}$ (ref.[82]), where N_p is the average number of photons per frame over the measurement. To ensure convergence of the fits, g_2 and g_6 were typically set to −450 and 450 nm.

Localization of the NPC scaffolds. The *x*, *y* and *z* coordinates and photon counts from the Thunderstorm analysis for all fluorescent spots were saved within an Excel spreadsheet ('raw image data.csv'). Regions of interest that contained spot clusters that probably arose from NPCs were saved in a text file ('cluster details.txt'). The Matlab script 'photonandz_filter' was used to curate the data, retaining only those localizations (Extended Data Fig. 2) with $z = 0 \pm 300$ nm, and for which the photon count was ≥3,000 (output file: 'roi_photon_filtered.txt').

Using 'circular_roi', the individual clusters were size selected, retaining only those with distributions wider than 59 nm and smaller than 153 nm (pairwise point distances 0.5 and 1.3 times the 118 nm camera pixel size, respectively). This process was simplified by plotting the points in a 11.8 nm pixel grid (one-tenth of the original camera pixels), for which the inter-spot distances were straightforward to determine visually. Clusters that were not round were also rejected, as they would not survive the circle-fitting algorithm used later. In practice, this process was straightforward to implement as usable clusters yielded circular shapes of a relatively consistent diameter. Occasional random spots not associated with clusters (background) were rejected, and closely spaced clusters were separated. The coordinates for all selected clusters were stored within the text file 'roi_all_combine.txt', and an image file 'all clusters.fig' (Extended Data Fig. 2c) was generated for visualization. Using 'separate_pores', the coordinates for individual clusters were extracted into separate text files.

The localizations in each of the individual clusters were then fit to a double-circle model, which reflected the double-ring structure of NUP96 within the NPC. Since the flatness of the NE suggested minimal tilt of the NPCs (see also Fig. 3), we assumed that the two circles were both parallel to the *xy* plane with centres defining an axis parallel to the *z* axis. The 'double-circle fit' algorithm minimized the sum of the absolute values of the residuals in the radial and *z* directions. The 'estimate_cylinder' script generated the *xyz* centroid, height and diameter of the cylinder defined by the best-fit double circle. The 'select_pores' script was used to select clusters that had at least 10 points with a diameter of 80–135 nm, a height of 40–65 nm and *z* centre of 0 ± 200 nm, according to the double-circle fit (Extended Data Fig. 2d). This double-circle fitting routine was a key step of the process to build the well-resolved NUP96 scaffold in Fig. 2.

To further improve the chosen localization datasets, outlier localizations were removed as follows. 'Circlefit_bisquare' was used to fit all cluster localizations to a circle in the *xy* plane, that is, ignoring the *z* values. Then, the mean distance to the circle for all localizations was determined (residuals), as well as the standard deviation of the residuals. Those localizations whose residual was more than two standard deviations away from the circle were eliminated, and the 'double-circle fit' and 'select_pores' scripts were re-run with the remaining points. In practice, very few clusters had points eliminated by this circle-fitting process. The localizations for all clusters were then combined based on their *xyz* centroid to yield the initial NPC scaffold (Fig. 2i,j).

Since the rotational orientation of NPCs in the NE is expected to be random, the alignment of clusters was expected to yield a double torus distribution, which it did (Fig. 2i,j). Although a non-flat angular distribution provides evidence of non-randomness (Extended Data Fig. 3b), this probably arises from undersampling ($N = 10$ nuclei) as it is difficult to explain how this could be recovered from different cells on different slides and days. To recover the eightfold rotationally symmetrical distribution of NUP96, the angles of the individual localizations relative to the centroid determined from the double-circle fit were estimated and binned (0–45°), assuming an eightfold periodicity. The distributions for each individual cluster were then fit to a sinusoidal function with a 45° period and a variable phase. The best-fit phase angle was then used to rotate the individual pore clusters about their *xyz* centroid, which were then all aligned based on their *xyz* centroids (Fig. 2k,l). This rotational algorithm was the second key step of the process to building the well-resolved NUP96 scaffold in Fig. 2. Considering the very low number of angle values (~13 on average; Extended Data Fig. 2e) placed in 9 bins, the fits were generally poor (Extended Data Fig. 3a). Nonetheless, the result of the rotated and centred individual clusters yielded well-isolated clusters that clearly revealed the expected eightfold rotational symmetry (Fig. 2k and Extended Data Fig. 3c).

Cargo localizations and the identification of tracks. As for the labelled nanobody localizations in the red channel, the multiple movies acquired for cargo trajectories were combined, and the *xyz* coordinates and photon counts for all fluorescent spots were identified via ThunderStorm (output file: 'all green spots.csv'). Due to the substantially faster imaging speed (2 or 3 ms versus 50 ms for the nanobody), the data were curated with 'photon_based_filter', retaining only those localizations for which the photon count was ≥1,000 (output file: 'spots_photon_filtered.txt'). To correct for the localization mis-match between the green and red channels, the *xyz* coordinates were corrected using the *xyz* alignment procedure described earlier using 'green_localization_in_red_channel' (output file: 'spots_photon_filtered_calib.txt'). After this coordinate correction, all cargo localizations within a 400-nm cube centred on a NPC centroid (from the double-circle fits of nanobody clusters) were identified using 'track_localize_whole_roi'. To align the cargo localizations with the averaged NPC scaffold, localizations were *xyz*-translated and then rotated based on the pore that they were closest to using 'centering_tracks_wrt_whole' and 'track_rotation_in_whole'. Cargo localizations identified in successive frames and linked to the same NPC were considered to represent the same molecule, and three successive localizations were linked to generate trajectories.

Statistics and reproducibility. No statistical method was used to predetermine sample sizes. Statistical methods, measurement precision, data included in the analysis and the repeatability of measurements are discussed throughout the text and supported by simulated data. The *N* values for all the reported measurements and simulations are indicated and defined within the figure legends.

Reporting Summary. Further information on research design is available in the Nature Research Reporting Summary linked to this article.

Data availability

Raw image and movie data are available from the corresponding author upon reasonable request. Source data are provided with this paper. All other data supporting the findings of this study are available within the paper and its supplementary information files.

Code availability

The Matlab scripts used to analyse the data are summarized in Supplementary Table 1 and are available at GitHub at https://github.com/npctat2021/npc3d2021.

References

68. Chowdhury, R., Sau, A. & Musser, S. M. Super-resolved 3D tracking of cargo transport through nuclear pore complexes by astigmatism imaging. *Protocol Exchange* https://doi.org/10.21203/rs.3.pex-1710/v1 (2022).
69. Kutay, U., Izaurralde, E., Bischoff, F. R., Mattaj, I. W. & Görlich, D. Dominant-negative mutants of importin-beta block multiple pathways of import and export through the nuclear pore complex. *EMBO J.* **16**, 1151–1163 (1997).
70. Görlich, D., Prehn, S., Laskey, R. A. & Hartmann, E. Isolation of a protein that is essential for the first step of nuclear protein import. *Cell* **79**, 767–778 (1994).
71. Ribbeck, K., Lipowsky, G., Kent, H. M., Stewart, M. & Görlich, D. NTF2 mediates nuclear import of Ran. *EMBO J.* **17**, 6587–6598 (1998).
72. Lyman, S. K., Guan, T., Bednenko, J., Wodrich, H. & Gerace, L. Influence of cargo size on Ran and energy requirements for nuclear protein import. *J. Cell Biol.* **159**, 55–67 (2002).
73. Yoshizawa, T. et al. Nuclear import receptor inhibits phase separation of FUS through binding to multiple sites. *Cell* **173**, 693–705 (2018).
74. Heim, R., Prasher, D. C. & Tsien, R. Y. Wavelength mutations and posttranslational autooxidation of green fluorescent protein. *Proc. Natl Acad. Sci. USA* **91**, 12501–12504 (1994).
75. Kent, H. M., Clarkson, W. D., Bullock, T. L. & Stewart, M. Crystallization and preliminary X-ray diffraction analysis for nuclear transport factor 2. *J. Struct. Biol.* **116**, 326–329 (1996).
76. Schwoebel, E. D., Talcott, B., Cushman, I. & Moore, M. S. Ran-dependent signal-mediated nuclear import does not require GTP hydrolysis by Ran. *J. Biol. Chem.* **273**, 35170–35175 (1998).
77. Débarre, D., J., B. M. & Wilson, T. Image based adaptive optics through optimization of low spatial frequencies. *Opt. Express* **15**, 8176–8190 (2007).
78. Berg, H. C. *Random Walks in Biology* (Princeton Univ. Press, 1993).
79. Kues, T., Peters, R. & Kubitscheck, U. Visualization and tracking of single protein molecules in the cell nucleus. *Biophys. J.* **80**, 2954–2967 (2001).
80. Schindelin, J. et al. Fiji: an open-source platform for biological-image analysis. *Nat. Methods* **9**, 676–682 (2012).
81. Fu, G., Tu, L.-C., Zilman, A. & Musser, S. M. Investigating molecular crowding within nuclear pores using polarization-PALM. *eLife* **6**, e28716 (2017).
82. Mortensen, K. I., Churchman, L. S., Spudich, J. A. & Flyvbjerg, H. Optimized localization analysis for single-molecule tracking and super-resolution microscopy. *Nat. Methods* **7**, 377–381 (2010).
83. Fischer, H., Polikarpov, I. & Craievich, A. F. Average protein density is a molecular-weight-dependent function. *Protein Sci.* **13**, 2825–2828 (2004).

Acknowledgements

We thank M. Rout, Y. M. Chook, M. S. Moore and D. Görlich for the LaG-9 anti-GFP nanobody, transportin, Imp α and Imp β expression plasmids, respectively, and J. Chao for assisting with the double-circle fit Matlab script. This research was supported by the National Institutes of Health (GM126190 to S.M.M.).

Author contributions

All authors contributed extensively to the work presented in this paper. S.M.M. conceived the approach. R.C. assembled and calibrated the AO 3D imaging system and wrote code. R.C. and A.S. installed the *z*-lock system, purified proteins, collected and analysed data and wrote the manuscript. S.M.M. developed the simulations, provided advice, analysed data and edited the manuscript.

Competing interests

The authors declare no competing interests.

Additional information

Extended data is available for this paper at https://doi.org/10.1038/s41556-021-00815-6.

Supplementary information The online version contains supplementary material available at https://doi.org/10.1038/s41556-021-00815-6.

Correspondence and requests for materials should be addressed to Siegfried M. Musser.

Peer review information *Nature Cell Biology* thanks Ulrich Kubitscheck, Michael Rout and the other anonymous reviewer for their contribution to the peer review of this work.

Reprints and permissions information is available at www.nature.com/reprints.

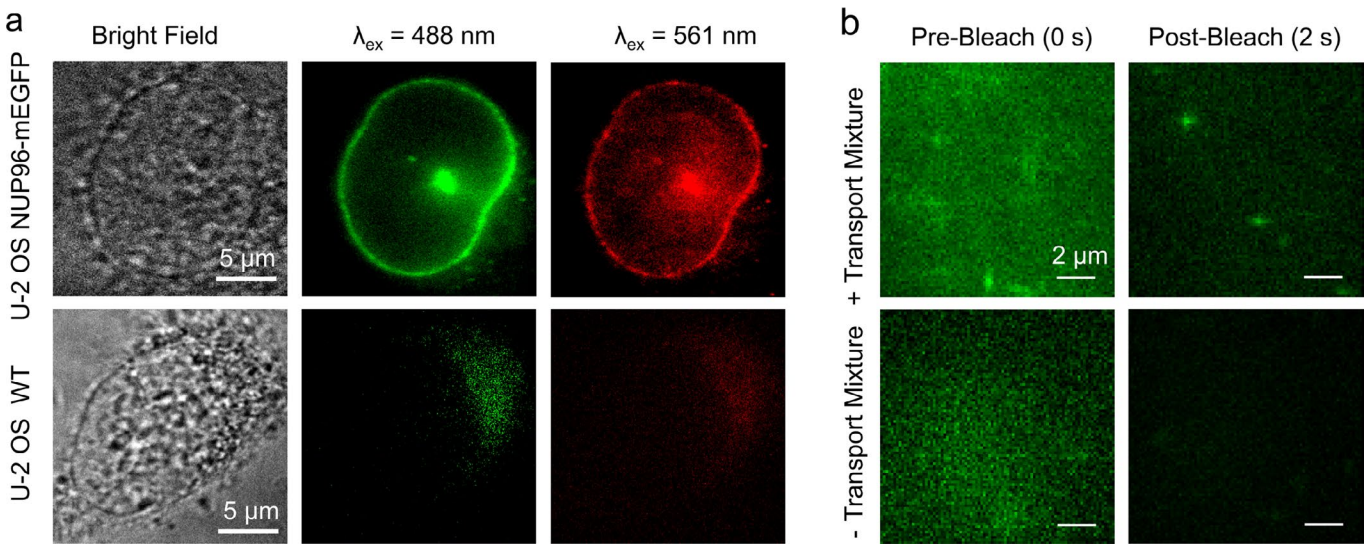

Extended Data Fig. 1 | Nanobody Specificity and Fluorescence Background. a, Specificity of the LaG-9 anti-GFP nanobody. Alexa568-labeled nanobody (100 nM) was added to permeabilized cells, incubated for 3 min and washed twice with IB + PVP. Cells were imaged at the nuclear equator. The top row shows the strong mEGFP fluorescence (λ_{ex} = 488 nm) obtained from the mEGFP-tagged NPCs of U-2 OS NUP96-mEGFP cells. The Alexa568 fluorescence (λ_{ex} = 561 nm) from the tagged nanobody matches the mEGFP fluorescence. In the bottom row, the wild type U-2 OS cells exhibited no fluorescence in the mEGFP channel and no nanobody binding. The range of the fluorescence images in the bottom row is 10 times smaller than in the top row, emphasizing the very low signal. These data indicate the high specificity of the nanobody for the mEGFP domain. Similar results were observed for $N = 20$ cells over 4 independent experiments. **b**, Fluorescence background and photobleaching of mEGFP. For all images, permeabilized U-2 OS NUP96-mEGFP cells labeled with HMSiR-labeled nanobodies were excited with λ_{ex} = 532 nm and emission was collected by a dual bandpass (545-623 nm, 656-763 nm). The mEGFP fluorescence (*left*) was photobleached after ~2 s of illumination, allowing diffusing M9-βGal(Atto542) cargo complexes to be readily visualized (*top right*). The HMSiR dye was not detectable (*bottom right*). Similar results were observed for $N = 20$ cells over 4 independent experiments.

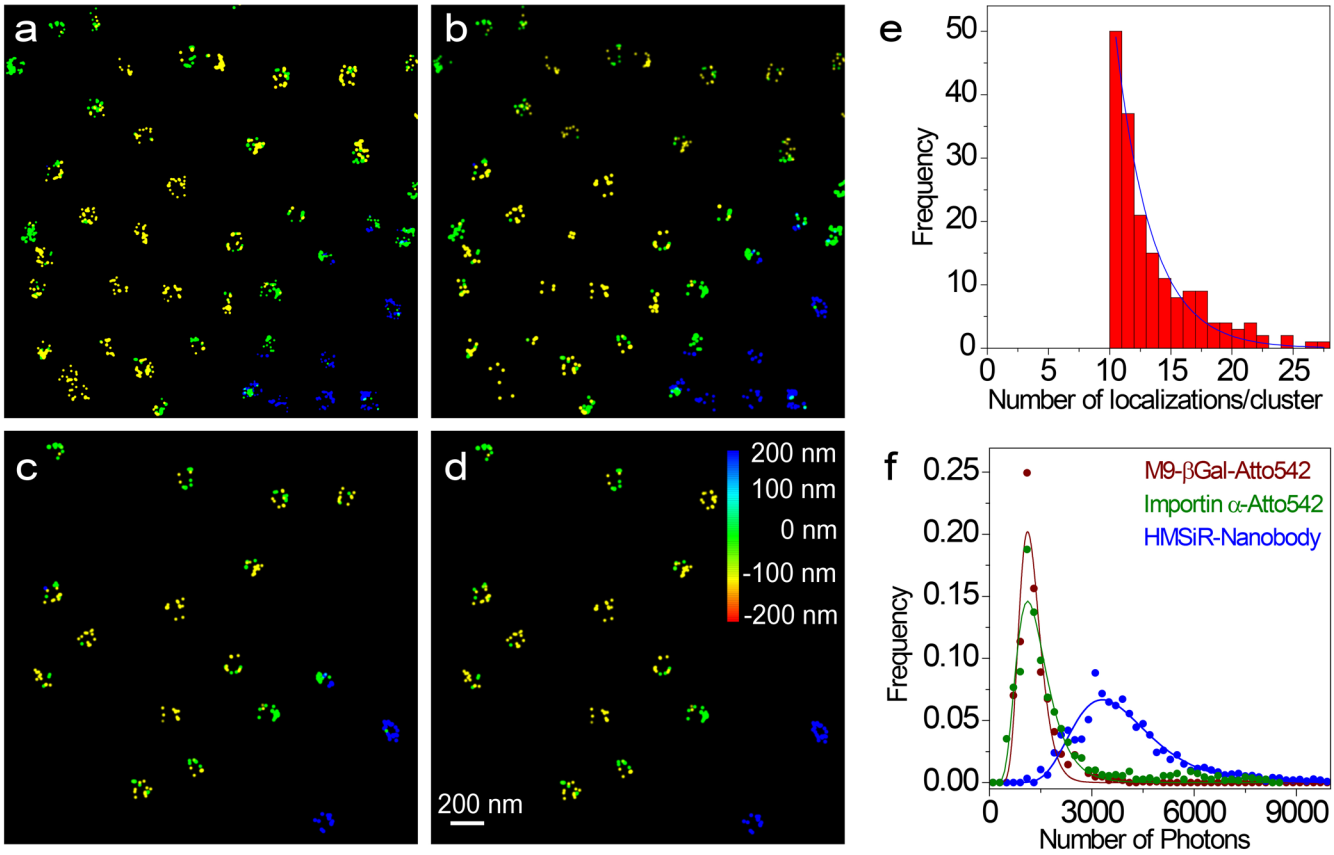

Extended Data Fig. 2 | Workflow for NPC Cluster Selection. a, Initial image obtained from ThunderSTORM. **b**, Image after photon filtering (≥ 3000 photons) and *z* filtering (0 ± 300 nm) (corresponds to Fig. 2e). **c**, Clusters remaining after applying a rough diameter threshold (59-153 nm) and with ≥ 10 localizations/cluster. **d**, Clusters remaining after the double-circle fit and subsequent curating (fit diameter = 80-135 nm; distance between the rings = 40-65 nm; *z*-centroid = 0 ± 200 nm). These remaining clusters are considered well-localized NPCs (image corresponds to Fig. 2h), and were used to construct the composite images in Fig. 2i–l. Dye localizations in **a**-**d** are color-coded based on *z*-height. **e**, Distribution of the number of localizations per cluster for the experiment in Fig. 2. The number of localizations per cluster followed an approximately exponential distribution (decay constant = 2.9) with an average of 13.2 following the filtering described in (**a-c**) and with a *z*-centroid = 0 ± 200 nm (N = 2362 total localizations obtained from 142 clusters from 10 nuclei; each nucleus was an independent biological replicate). **f**, Photon frequency histograms. The HMSiR-labeled nanobody was bound to NPCs (Fig. 2) and the Atto542-labeled M9-βGal and Imp α were undergoing transport (Figs. 4 and 5). The log-normal fit parameters were used for the simulations in Supplementary Data 1 (software file 1) and Supplementary Data 2 (software file 2). Source numerical data are provided in source data.

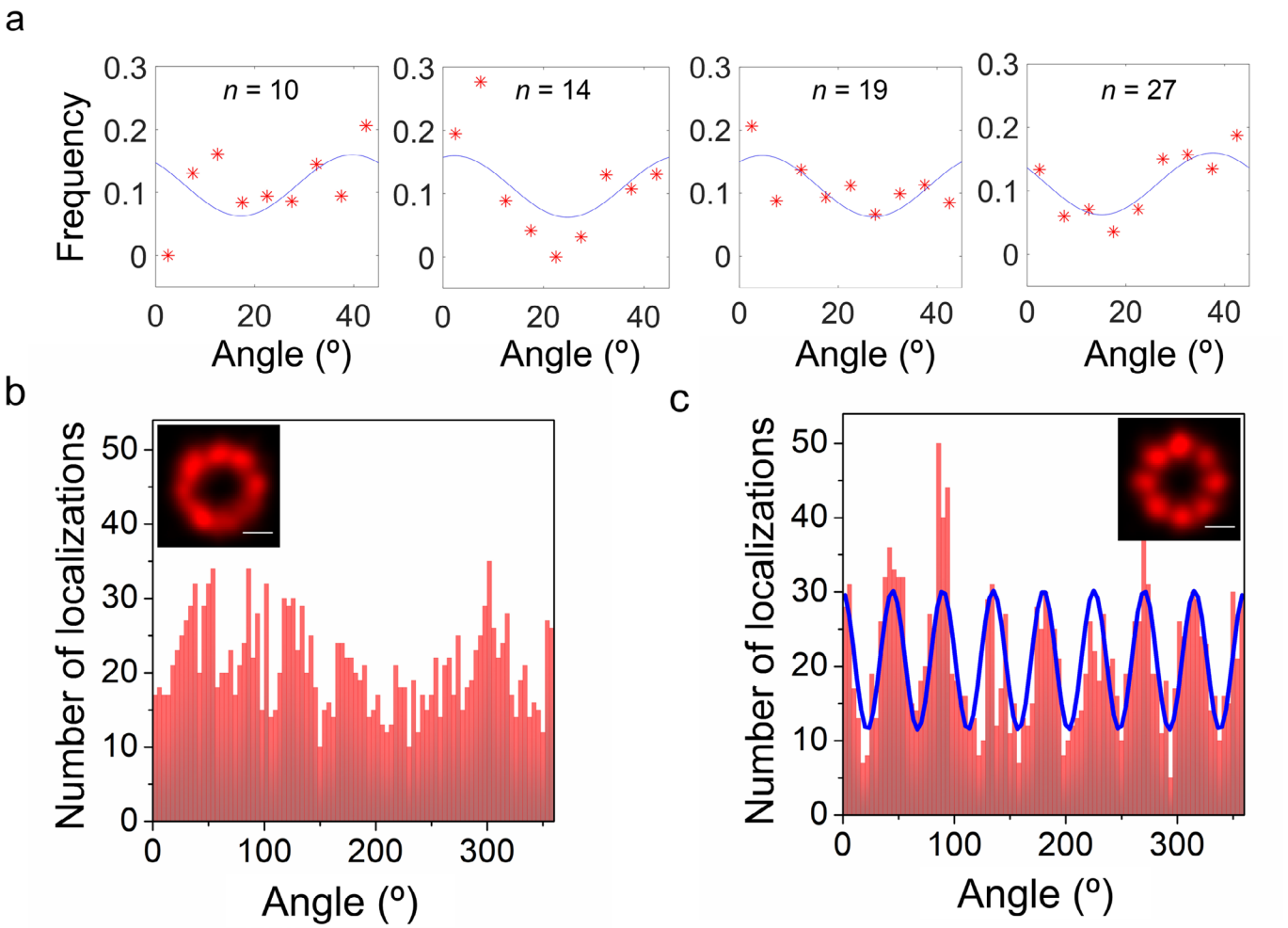

Extended Data Fig. 3 | Rotation of Individual NPC Clusters. a, Estimating the rotational phase angle (φ). The angles of individual localizations relative to the double-circle centroid of well-localized NPC clusters (Extended Data Fig. 2d) were estimated and binned (5° bins, θ = 0-45°). Four examples are shown here for a range of localizations/cluster (the number of localizations/cluster, *n*, is given in each figure panel). Distributions were fit to $y=1/9+(1/20.6)*\cos[8(\theta-\varphi)]$. The 1/9 term reflects the 9 bins, and the cosine scaling factor is a reasonable average based on simulations. This amplitude scaling factor is insensitive to the goodness-of-fit due to orthogonality – the phase angle shifts the curve laterally, and identical phase angles are obtained by the fitting routine regardless of the scaling factor. The fixed scaling factor enables rapid convergence of the fit. The phase angles from these fits were used to rotate pore clusters before aligning them based on their centroids. **b**, Angular distribution of localizations in the initially aligned pore clusters (Fig. 2i). Inset: Fig. 2i, bar: 50 nm. **c**, Angular distribution of rotationally-corrected localizations (Fig. 2k). Inset: Fig. 2k, bar: 50 nm. Pore clusters were rotated based on the phase angle as determined in (**a**) before aligning. The distribution was fit to $y=y_0+c_1*\sin(8(x-\phi))$, where y_0, c_1 and ϕ are fit parameters. The minima define the angles of the dashed spokes in Fig. 2m. Source numerical data are provided in source data.

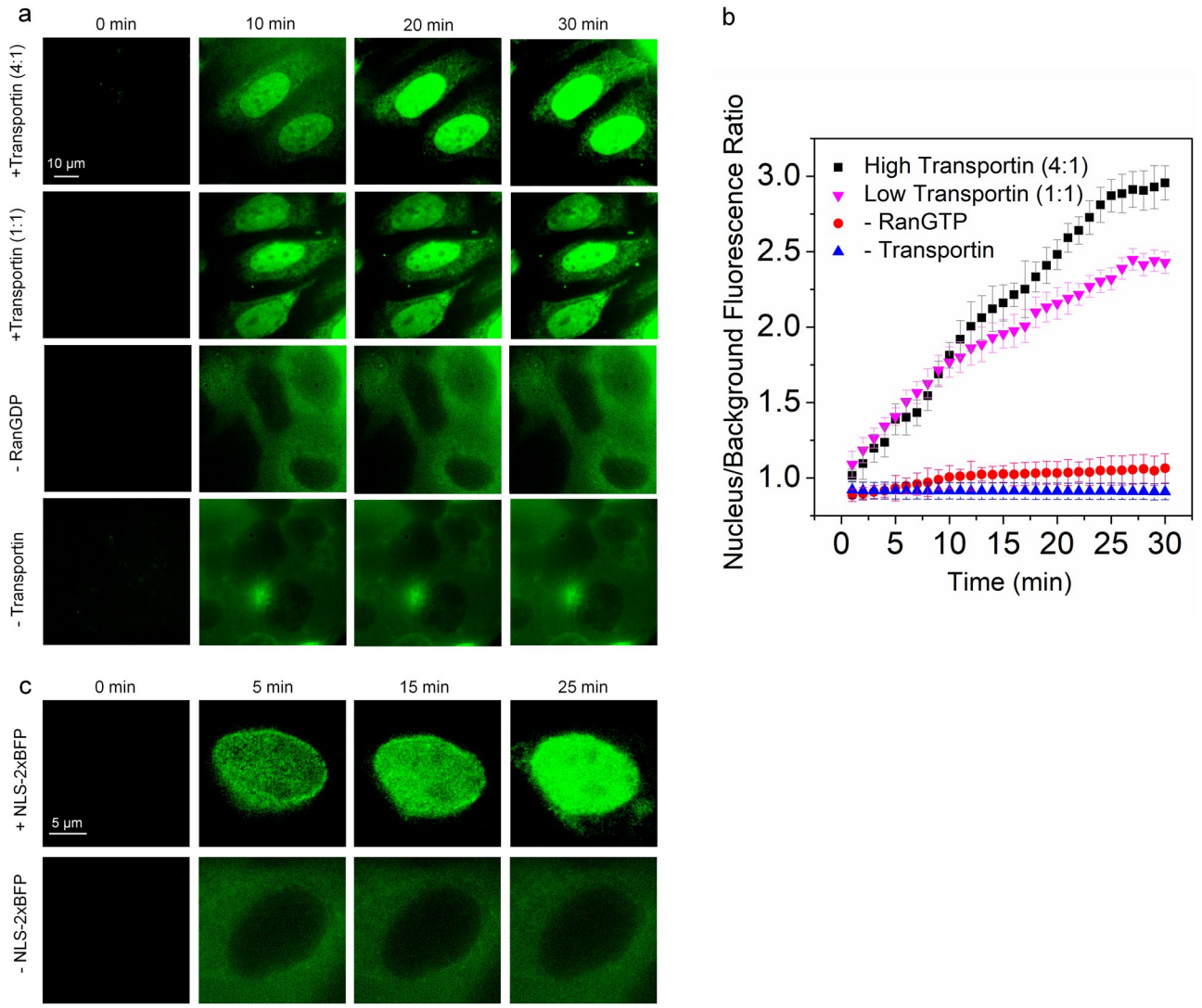

Extended Data Fig. 4 | Nuclear Accumulation of M9-βGal and Imp α in Permeabilized U-2 OS NUP96-mEGFP Cells. a, Nuclear import of M9-βGal(Atto542). The M9-βGal cargo is an ~500 kDa tetramer with four M9 nuclear localization sequences (NLSs) that are recognized by the transportin NTR. Transport reactions were monitored using wide-field fluorescence (λ_{ex} = 532 nm) in the presence or absence of transportin or RanGTP (RanGDP + GTP) as indicated. The 'transport mix' was flowed in at t = 0.5 min. Representative images from four time points are shown (N = 20 cells from 4 independent experiments). [M9-βGal] = 0.25 μM, [transportin] = 0.25 or 1.0 μM, [RanGDP] = 0.5 μM, [NTF2] = 1 μM, [GTP] = 1 mM. **b**, Kinetics of nuclear import of M9-βGal. Average nuclear fluorescence (±s.d.) was quantified over time for N = 15 (-transportin), 17 (-RanGTP), or 20 (high and low transportin) cells from 4 independent experiments). Background refers to an area far from the cells. **c**, Cargo-dependent nuclear uptake of Imp α. Robust accumulation of Imp α(Atto542) into the nucleus (λ_{ex} = 532 nm) occurs in the presence of the NLS-2xBFP cargo (*top row*) but not in its absence (*bottom row*). The range of the fluorescence images in the bottom row is 5 times smaller than in the top row, emphasizing the very low nuclear accumulation (N = 18 cells over 4 independent experiments). [Imp α(Atto542)] = 0.5 μM, [Imp β] = 0.5 μM, [NLS-2xBFP] = 0.5 μM, [RanGDP] = 1.5 μM, [NTF2] = 1 μM and [GTP] = 1 mM. Source numerical data are provided in source data.

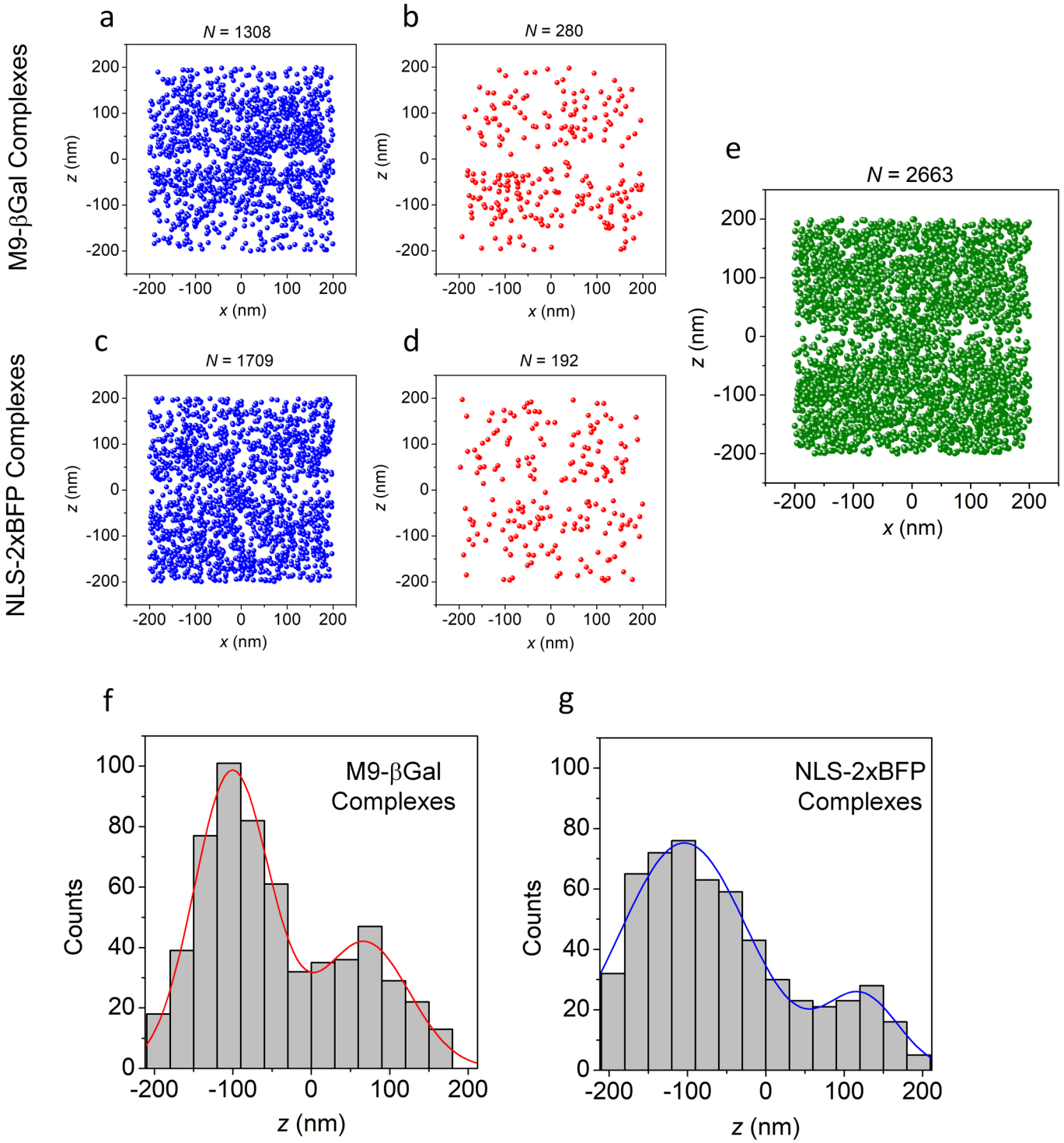

Extended Data Fig. 5 | Localizations of M9-βGal and NLS-2xBFP Complexes. a,b, Brief M9-βGal complex appearances. Shown are the localizations from Fig. 4a that remained visible for one (**a**) or two (**b**) 3 ms frames. The *N* values are the number of localizations from 142 NPCs from 10 nuclei; each nucleus was an independent biological replicate. **c,d**, Brief NLS-2xBFP complex appearances. Shown are the localizations from the experiment in Fig. 5 that remained visible for one (**c**) or two (**d**) 2 ms frames. The *N* values are the number of localizations from 115 NPCs from 10 nuclei; each nucleus was an independent biological replicate. Localizations shown in (**a-d**) appear randomly distributed, consistent with particles that are largely diffusing and not interacting with the NPC. **e**, Simulated distribution of particles penetrating a barrier. In this simulation [Supplementary Data 2 (software file 2)], particles appeared randomly within two compartments separated by a 50 nm thick barrier with a 100 nm diameter pore. This distribution models the M9-βGal complex localizations in Fig. 4a. The localizations appearing within the barrier result from the precision error, indicating that the localizations observed within the NE region in Fig. 4a are likely a consequence of localization error. **f,g**, Localizations along the transport axis. Distribution of *z* values for M9-βGal complexes (**f**; from Fig. 4e,f) and NLS-2xBFP complexes (**g**; from Fig. 5e,f) undergoing import or abortive import. Distributions are fit to a double Gaussian function yielding mean values (±s.d.) of −100 ± 48 nm and 68 ± 56 nm for M9-βGal complexes, and −104 ± 82 nm and 122 ± 47 nm for NLS-2xBFP complexes. Source numerical data are provided in source data.

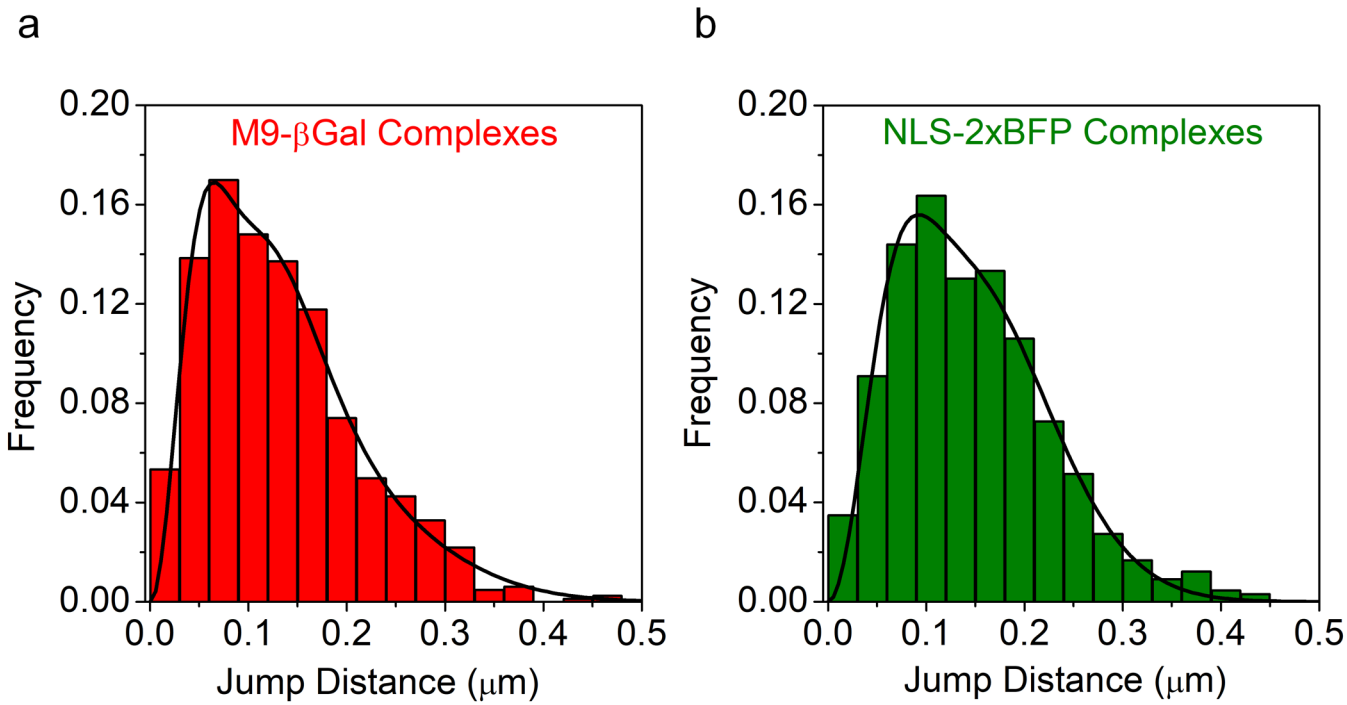

Extended Data Fig. 6 | Cargo Complex Diffusion Constants. a, 3D step-size histogram for M9-βGal complexes. Step sizes of M9-βGal complexes were calculated from consecutive localizations in the trajectories of Fig. 4c ($N = 824$ total jump distances from 10 nuclei; each nucleus was an independent biological replicate). Data were fit using Eq. 4, yielding three distinct diffusion constants of 0.2 (18%), 0.8 (50%) and 2.6 (32%) $\mu m^2/s$, or a weighted average diffusion constant of 1.3 $\mu m^2/s$. **b**, 3D step-size histogram for NLS-2xBFP complexes. Step sizes of NLS-2xBFP complexes were calculated from consecutive localizations in the trajectories of Fig. 5c ($N = 660$ total jump distances from 10 nuclei; each nucleus was an independent biological replicate). Fitting the histogram yielded two distinct diffusion constants of 0.6 (25%) and 2.7 (75%) $\mu m^2/s$, or a weighted average diffusion constant of 2.2 $\mu m^2/s$. Due to the highly confined, irrregular volume sampled by the cargo complexes, these average diffusion constant estimates are considered both approximate and an underestimate. For comparison, the diffusion constant of the M9-βGal and NLS-2xBFP cargo complexes in aqueous buffer are approximated as ~34 and 55 $\mu m^2/s$, respectively, using the Stokes-Einstein equation and a protein density of ~1.35 g/cm^3 (ref. [83]). Source numerical data are provided in source data.

nature portfolio

Corresponding author(s): Siegfried Musser

Last updated by author(s): Oct 26, 2021

Reporting Summary

Nature Portfolio wishes to improve the reproducibility of the work that we publish. This form provides structure for consistency and transparency in reporting. For further information on Nature Portfolio policies, see our Editorial Policies and the Editorial Policy Checklist.

Statistics

For all statistical analyses, confirm that the following items are present in the figure legend, table legend, main text, or Methods section.

n/a	Confirmed
☐	☒ The exact sample size (*n*) for each experimental group/condition, given as a discrete number and unit of measurement
☐	☒ A statement on whether measurements were taken from distinct samples or whether the same sample was measured repeatedly
☒	☐ The statistical test(s) used AND whether they are one- or two-sided *Only common tests should be described solely by name; describe more complex techniques in the Methods section.*
☒	☐ A description of all covariates tested
☐	☒ A description of any assumptions or corrections, such as tests of normality and adjustment for multiple comparisons
☐	☒ A full description of the statistical parameters including central tendency (e.g. means) or other basic estimates (e.g. regression coefficient) AND variation (e.g. standard deviation) or associated estimates of uncertainty (e.g. confidence intervals)
☒	☐ For null hypothesis testing, the test statistic (e.g. *F*, *t*, *r*) with confidence intervals, effect sizes, degrees of freedom and *P* value noted *Give P values as exact values whenever suitable.*
☒	☐ For Bayesian analysis, information on the choice of priors and Markov chain Monte Carlo settings
☒	☐ For hierarchical and complex designs, identification of the appropriate level for tests and full reporting of outcomes
☒	☐ Estimates of effect sizes (e.g. Cohen's *d*, Pearson's *r*), indicating how they were calculated

Our web collection on statistics for biologists contains articles on many of the points above.

Software and code

Policy information about availability of computer code

Data collection	Data collection was performed on microscopes as detailed in the manuscript using: Metamorph 7.7.7, CasAO 1.0, MicAO 1.3, LabView 2015 (Zeiss 200 M; 3D single molecule microscope) NIS-Elements AR 5.02.01 (Nikon Eclipse Ti; wide-field microscope)
Data analysis	Data were curated and analyzed with custom code written in Matlab R2018a, as detailed in the manuscript. The Matlab scripts used to analyze the data are summarized in Supplementary Table 1, and are available at GitHub under https://github.com/npctat2021/npc3d2021. The following software packages were used for visualization, analysis, data presentation, and simulations: ImageJ (Fiji 1.52P) Origin 8.5 Kaleidagraph 4.5.2 Microsoft Excel 16.16.20 (200307) SnapGene 5.3.2

For manuscripts utilizing custom algorithms or software that are central to the research but not yet described in published literature, software must be made available to editors and reviewers. We strongly encourage code deposition in a community repository (e.g. GitHub). See the Nature Portfolio guidelines for submitting code & software for further information.

Data

Policy information about availability of data

All manuscripts must include a data availability statement. This statement should provide the following information, where applicable:

- Accession codes, unique identifiers, or web links for publicly available datasets
- A description of any restrictions on data availability
- For clinical datasets or third party data, please ensure that the statement adheres to our policy

Raw image and movie data are available from the corresponding author upon reasonable request. Plasmids encoding the transport cargos and nanobody used are available from Addgene (ID#s 172489, 172490 and 176151) and their SnapGene files are included as Supplementary Data 3. All other data supporting the findings of this study are available within the paper and its supplementary information files. Source data are provided with this paper.

Field-specific reporting

Please select the one below that is the best fit for your research. If you are not sure, read the appropriate sections before making your selection.

☒ Life sciences ☐ Behavioural & social sciences ☐ Ecological, evolutionary & environmental sciences

For a reference copy of the document with all sections, see nature.com/documents/nr-reporting-summary-flat.pdf

Life sciences study design

All studies must disclose on these points even when the disclosure is negative.

Sample size	Sample size was not pre-determined. NPC scaffold data were compared with Monte Carlo simulations of similar dataset sizes to estimate errors. The non-random nature of cargo trajectory data was obvious by inspection, and the characteristics of the observed distributions are described.
Data exclusions	Nanobody localizations were excluded if they were in a cluster of < 10. Clusters were defined by previously published constraints, and cluster number was empirically determined as a minimum necessary to reproduce the known NPC double ring structure. For cargo transport conduits, localizations were excluded for trajectories < 3 points as simulations indicated that this was determined necessary to remove spurious points.
Replication	NPC scaffold and cargo transport datasets were each obtained from 10 nuclei, which represent independent biological replicates. NPC scaffold structures were obtained twice, and these were reproducible (compared in Table 1). Cargo transport conduits for two different transport receptors were obtained once each and these overlapped.
Randomization	This is not relevant to this study. Single molecule fluorescence spots appeared randomly by design (stochastic blinks or diffused into view). All data were analyzed as a whole, and not separated into comparison groups. Data analysis took into account this randomness by comparing to Monte Carlo simulations of the datasets.
Blinding	Data were independently analyzed by at least two individuals in multiple stages.

Reporting for specific materials, systems and methods

We require information from authors about some types of materials, experimental systems and methods used in many studies. Here, indicate whether each material, system or method listed is relevant to your study. If you are not sure if a list item applies to your research, read the appropriate section before selecting a response.

Materials & experimental systems

n/a	Involved in the study
☐	☒ Antibodies
☐	☒ Eukaryotic cell lines
☒	☐ Palaeontology and archaeology
☒	☐ Animals and other organisms
☒	☐ Human research participants
☒	☐ Clinical data
☒	☐ Dual use research of concern

Methods

n/a	Involved in the study
☒	☐ ChIP-seq
☒	☐ Flow cytometry
☒	☐ MRI-based neuroimaging

Antibodies

Antibodies used	The anti-GFP nanobody LaG-9 reported previously (Fridy, et al. 2014, Nat. Meth. 11:1253) was purified after overproduction in Escherichia coli and used at the concentration indicated in the Method section.

Validation	The anti-GFP LaG-9 nanobody was validated by comparing binding to a GFP-tagged human cell line relative to its untagged control, as shown in Extended Data Fig. 1a.

Eukaryotic cell lines

Policy information about cell lines

Cell line source(s)	U-2 OS-CRISPER-NUP96-mEGFP clone#195 (300174 from CLS GmbH) U-2 OS (300364 from CLS GmbH)
Authentication	Used without authentication.
Mycoplasma contamination	Tested monthly for mycoplasma contamination. No contamination was observed during the study period.
Commonly misidentified lines (See ICLAC register)	None.